SANDIA REPORT
SAND2022-13382
Printed September 2022

Sandia National Laboratories

Processing, structure, and thermal properties of ZrW_2O_8, HfW_2O_8, $HfMgW_3O_{12}$, $Al(HfMg)_{0.5}W_3O_{12}$, and $Al_{0.5}Sc_{1.5}W_3O_{12}$ negative and zero thermal expansion coefficient ceramics

Sean R. Bishop, Dan R. Lowry, Amanda S. Peretti, Mia A. Blea-Kirby, Perla A. Salinas, Eric N. Coker, Edward R. Arata, Mark A. Rodriguez, Shannon E. Murray, Jacob T. Mahaffey, and Laura B. Biedermann

Prepared by
Sandia National Laboratories
Albuquerque, New Mexico
87185 and Livermore,
California 94550

Issued by Sandia National Laboratories, operated for the United States Department of Energy by National Technology & Engineering Solutions of Sandia, LLC.

Available to DOE and DOE contractors from
U.S. Department of Energy
Office of Scientific and Technical Information
P.O. Box 62
Oak Ridge, TN 37831

Telephone: (865) 576-8401
Facsimile: (865) 576-5728
E-Mail: reports@osti.gov
Online ordering: http://www.osti.gov/scitech

Available to the public from
U.S. Department of Commerce
National Technical Information Service
5301 Shawnee Rd
Alexandria, VA 22312

Telephone: (800) 553-6847
Facsimile: (703) 605-6900
E-Mail: orders@ntis.gov
Online order: https://classic.ntis.gov/help/order-methods/

ABSTRACT

Negative and zero coefficient of thermal expansion (CTE) materials are of interest for developing polymer composites in electronic circuits that match the expansion of Si and in zero CTE supports for optical components, e.g., mirrors. In this work, the processing challenges and stability of ZrW_2O_8, HfW_2O_8, $HfMgW_3O_{12}$, $Al(HfMg)_{0.5}W_3O_{12}$, and $Al_{0.5}Sc_{1.5}W_3O_{12}$ negative and zero thermal expansion coefficient ceramics are discussed. $Al_{0.5}Sc_{1.5}W_3O_{12}$ is demonstrated to be a relatively simple oxide to fabricate in large quantity and is shown to exhibit single phase up to 1300 ^oC in air and inert N_2 environments. The negative and zero CTE behavior was confirmed with dilatometry. Thermal conductivity and heat capacity were reported for the first time for $HfMgW_3O_{12}$ and $Al_{0.5}Sc_{1.5}W_3O_{12}$ and thermal conductivity was found to be very low (~0.5 W/mK). Grüneisen parameter is also estimated. Methods for integration of $Al_{0.5}Sc_{1.5}W_3O_{12}$ with other materials was examined and embedding 50 vol% of the ceramic powder in flexible epoxy was demonstrated with a commercial vendor.

ACKNOWLEDGEMENTS

Nichole Valdez (1819) for assistance with XRD, Luis Jauregui (1819) for SEM measurements, Kevin Strong (1851) and Thomas Diebold (1851) for tungstate water quenching studies and RUS measurements, Andrew Smith (1816) for TGA measurements, and Eric Neuman (7568) for discussions of powder processing. The authors also acknowledge financial support from the LDRD office RAD mission campaign.

CONTENTS

LIST OF FIGURES

LIST OF TABLES

This page left blank

ACRONYMS AND TERMS

Acronym/Term	Definition
d_{90}	90% particles less than this diameter
CTE	Coefficient of thermal expansion
ρ	Density
DSC	Differential scanning calorimetry
DTA	Differential thermal analysis
γ	Grüneisen parameter
C_p	Heat capacity at constant pressure
C_v	Heat capacity at constant volume
HTXRD	High temperature X-ray diffraction
V	Molar volume
v	Poisson's ratio
PVB	Polyvinyl butyral
RUS	Resonant ultrasound spectroscopy
SEM	Scanning electron microscopy
G	Shear elastic modulus
SS316	Stainless steel 316
ρ_{Theor}	Theoretical density
κ	Thermal conductivity
α_T	Thermal diffusivity
TGA	Thermogravimetric analysis
α	Volumetric CTE
XRD	X-ray diffraction
YSZ	Yttria-stabilized zirconia
E	Young's elastic modulus

1. INTRODUCTION

Negative and zero coefficient of thermal expansion (CTE) materials are of interest for developing polymer composites in electronic circuits that match the expansion of Si and in zero CTE supports for optical components, e.g., mirrors [1, 2]. Negative CTE is believed to occur from concerted tilting of polyhedra that lead to a reduction of second-nearest-neighbor distances [2, 3]. In this work, cubic tungstates (ZrW_2O_8 and HfW_2O_8) which exhibit isotropic negative CTE and non-cubic tungstates ($HfMgW_3O_{12}$, $Al(HfMg)_{0.5}W_3O_{12}$, and $Al_{0.5}Sc_{1.5}W_3O_{12}$) which exhibit anisotropic, but near zero volumetric CTE are examined.

1.1. ZrW_2O_8 and HfW_2O_8

ZrW_2O_8 and HfW_2O_8 are cubic and thus exhibit negative CTE equally in all crystal directions. The CTE of ZrW_2O_8 from sub-ambient to 777 ^oC has been reported to be -9 ppm/^oC [3]. The cubic phase is thermodynamically stable above ~1105 ^oC [4], but is often kinetically frozen-in to room temperature by quenching. Annealing at ~>800 ^oC results in decomposition [3]. Upon heating the cubic phase from room temperature there is an order/disorder phase transition at 160 – 180 ^oC which leads to a change in the CTE, though it remains negative up to the decomposition temperature. The materials melt at 1260 – 1280 ^oC, which given the cubic phase formation temperature of 1105 ^oC, yields a narrow processing range for solid state reactions [4]. Alternatively, ZrW_2O_8 has been fabricated using a sol-gel approach involving dehydration of a low temperature fabricated phase at 500 ^oC to form the desired cubic oxide phase [5]. Less studies are available on HfW_2O_8 though behavior, if not indicated above, is expected to be similar to ZrW_2O_8.

1.2. $HfMgW_3O_{12}$, $Al(HfMg)_{0.5}W_3O_{12}$, and $Al_{0.5}Sc_{1.5}W_3O_{12}$

$HfMgW_3O_{12}$, $Al(HfMg)_{0.5}W_3O_{12}$, and $Al_{0.5}Sc_{1.5}W_3O_{12}$ exhibit anisotropic expansion, but with a volumetric expansion near zero. $HfMgW_3O_{12}$ may be the least stable due to hygroscopic Mg, which the Al substitution in $Al(HfMg)_{0.5}W_3O_{12}$ is believed to mitigate [6]. $Al_{0.5}Sc_{1.5}W_3O_{12}$ exhibits significantly improved stability as shown in this project and has shown near zero CTE from sub-ambient to 1100 ^oC [7] and has been investigated previously for infrared transparent windows [8]. A variety of other near zero, negative, and positive CTE materials based on this same class of materials exists, though many have poor stability as described in the literature [9]. The anisotropic expansion leads to significant strain between the crystals or grains that can result in micro-cracking [10].

2. POWDER AND BULK PROCESSING

2.1. Materials

The starting oxide powders used in this project are listed in Table 1. Starting particle sizes measured in this project for the powders are described in Appendix A. The tungstate oxides fabricated in this project, their molecular weight (MW), theoretical density (ρ_{Theor}), and crystal structure are reported in Table 2.

Table 1: Powder sources

Material	Source	Part Number
ZrO_2	US Research Nanomaterials	US1018M (1 μm)
WO_3	US Research Nanomaterials	US1144M (4 μm)
HfO_2	Alfa Aesar	40270 (Lot: Z27E052)
Al_2O_3	Alcoa	A14-325
Sc_2O_3	Legacy 1816 powder "Garino source"	N/A
MgO	US Research Nanomaterials	US1130M (300 nm)

Table 2: Molecular weight, theoretical density, and structure of studied tungstates

Material	MW [g/mol]	ρ_{Theor} [g/cm^3]	Structure
α-ZrW_2O_8	586.9	5.071 [10]	Cubic, $P2_13$
HfW_2O_8	674.2	5.888 [11]	Cubic, $P2_13$
$HfMgW_3O_{12}$	946.3	5.201 [12]	Orthorhombic, $Pna2_1$
$Al(HfMg)_{0.5}W_3O_{12}$	871.9	5.2859 [13]	Orthorhombic, Pbcn
$Al_{0.5}Sc_{1.5}W_3O_{12}$	824.4	4.6424 [13]	Orthorhombic, Pbcn

2.2. ZrW_2O_8 and HfW_2O_8

As described in the introduction, ZrW_2O_8 and HfW_2O_8 form the desired negative thermal expansion cubic phase above ~1105 °C, and need to be quenched to freeze-in the cubic phase to room temperature. For this project, large quantities (> 1 kg) were desired and in most cases high temperature sintered dense bulk bodies were needed. Therefore the quenching from high temperature process, which may be more readily scalablethan sol-gel, and which also can produce dense bodies, was selected.

The final process used for fabricating ZrW_2O_8 powders is described here. Powders were fabricated by ball milling oxides of ZrO_2 with WO_3 using 5 mm cylindrical YSZ media in water for ~ 7 days to break down the large starting particles (~5 µm ZrO_2 and 10 µm WO_3) to ~0.1 µm and then dried in a pan on a hot plate (particle size and milling details are in appendix). After drying, the powders were pressed uniaxially without binder into ~1.25" diameter by ¼" thick pellets and placed on a Pt sheet on an alumina setter inside a tube furnace (tungstates were found to be very reactive with alumina setters, forming low melting temperature phases). Three pellets at a time were placed in the furnace and calcined at 1160 °C for 4 h and then pushed out of the furnace with a mullite rod onto a setter underneath a fan, as shown in Figure 1.

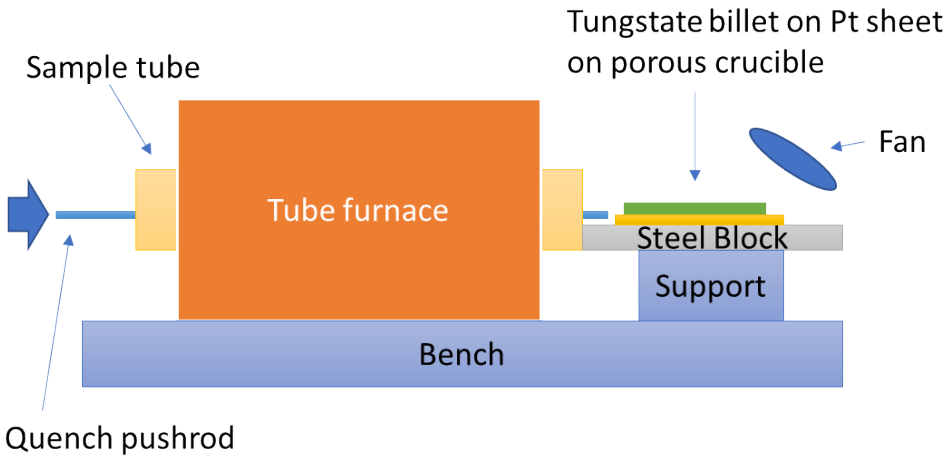

Figure 1: Schematic of tube furnace quench setup.

Quantifying the amount of cubic phase consistently proved challenging, due in part to the possible formation of low symmetry orthorhombic ZrW_2O_8 with many overlapping diffraction peaks, particularly with ZrO_2. The highest cubic phase fraction obtained is ~95 wt%, with ZrO_2, WO_3, and orthorhombic ZrW_2O_8 attributed to impurities, as shown by the diffraction pattern in Figure 2. The relative peak heights for WO_3 at ~23.5° and ~24.5° and cubic ZrW_2O_8 at ~22° serve as qualitative metrics for identifying relative purity. Longer anneals (12 h) and at higher (up to 1220 °C) and lower (1130 °C) annealing temperatures were examined and not consistently found to improve purity. It is worth noting that the materials are expected to melt at ~1230 – 1280 °C. Quenching into a water bath by dropping the sample in a vertical tube furnace into water was also performed, but not found to improve purity. Larger pellets (~2.5 in. diameter) were also briefly attempted with air quenching but low purity was obtained, possibly due to the larger volume of material resulting in a slower quench rate. As mentioned above, interpreting XRD data was challenging and there is low confidence in purity determination. In all cases, though, WO_3 impurity peaks as described above were observed. HfW_2O_8 powders were made in a similar manner, though far less material was fabricated. In this project, over 1 kg of ZrW_2O_8 was fabricated in the above method. However, 100% single phase was never clearly obtained, indicating a significant challenge to make this material in a bulk form. If only a powder form is desired, chemical routes described earlier may be a more feasible solution. Additionally, for smaller bulk samples than made here, single phase has been reported in the literature using quench methods [14].

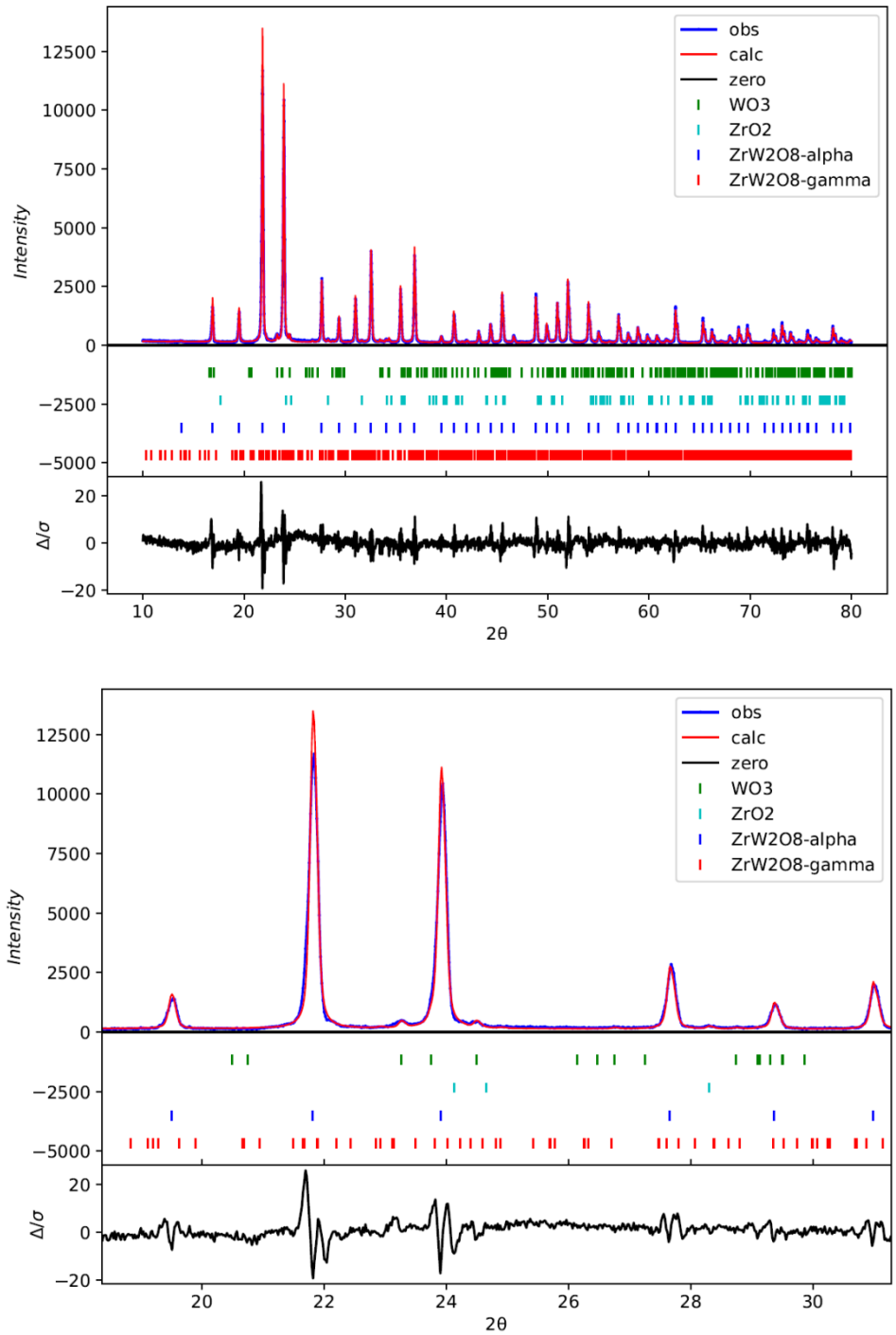

Figure 2: XRD pattern for ZrW_2O_8 showing full scan (top) and scan with smaller range (bottom). The smaller range scan shows where characteristic impurity peaks of WO_3 can commonly be observed at ~23° and 24.5° bracketing the strong α-ZrW_2O_8 peak at ~23.8°. 95 wt% α-ZrW_2O_8, 1 wt% γ-ZrW_2O_8, 1 wt% ZrO_2, and 3 wt% WO_3 is estimated from the fit. (Data name: 2022-0011-503-AP ZrW2O8 air)

After calcining the pellets, they were either handed off for milling operations for thermal spray or aerosol deposition, or ground and milled and then pressed into a pellet and sintered again in the same conditions as above for thermal analysis measurements. It is worth noting that the milling operation, particularly high energy milling used for aerosol deposition powder fabrication resulted in amorphization of the powder. These results are not unexpected given the low pressures leading to amorphization (~1.5 – 3 GPa from quasistatic and dynamic compression [15]) and likely due to the metastability of the material.

A scanning electron microscopy (SEM) image of a cross-sectioned polished surface of a sintered ZrW_2O_8 pellet is shown in Figure 3. Significant porosity is observed resulting in a density of ~90% with grain size ~10 – 30 μm [15] (large but expected given sintering conditions close to the melting temperature). Some microcracking is observed in the image which may have occurred from quenching the material.

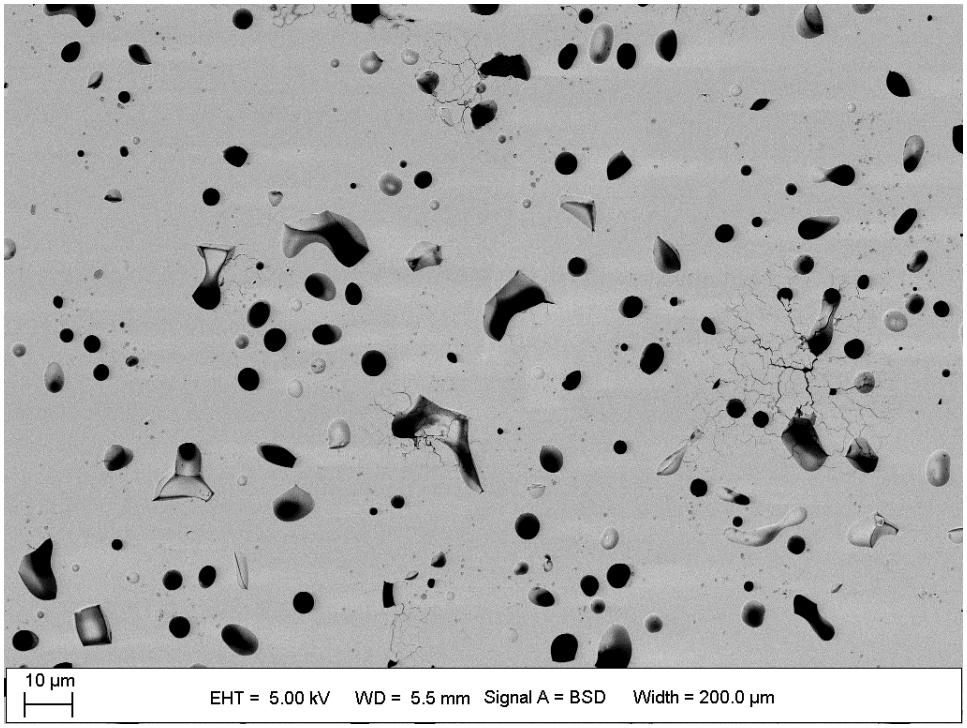

Figure 3: SEM image of a sintered ZrW_2O_8 pellet [15]

2.3. $Al_{0.5}Sc_{1.5}W_3O_{12}$, $Al(HfMg)_{0.5}W_3O_{12}$, and $HfMgW_3O_{12}$

Unlike the cubic tungstates above, $Al_{0.5}Sc_{1.5}W_3O_{12}$, , $Al(HfMg)_{0.5}W_3O_{12}$, and $HfMgW_3O_{12}$ are not metastable materials as described in the introduction, and therefore do not require quenching. The powder fabrication process is similar to the cubic tungstates above (except Mg containing materials were ball milled with isopropyl alcohol instead of water). For the final 1 kg batch of $Al_{0.5}Sc_{1.5}W_3O_{12}$, precursor oxides ($Al_2O_3$, Sc_2O_3, and WO_3) were ball milled for ~5 days using 5 mm cylindrical media, and then pressed into pellets and calcined on Pt sheets at 1160 ^oC (4 h), and cooled at 10 ^oC/min to room temperature. After calcination, the samples formed dense disks that were first crushed to ~1/4 in. or less size pieces using a hammer and die (with weigh papers separating metal components from the oxide to reduce contamination), followed by dry milling the powder in a

turbula mill with 20 mm diameter YSZ media for ~15-30 min intervals followed by passing powder through an 850 μm sieve. Powder that did not pass through the sieve was re-run on the turbula mill, with additional chunks of tungstate added. Once sufficient powder passed through the sieve, it was then wet ball milled with water with 5 mm cylindrical YSZ media for ~7 days. Particle size information is shown in A.3. The powder was then mixed with 2 wt% PVB binder (using acetone and mortar and pestle) and uniaxially pressed at 10 ksi followed by 30 ksi isostatic pressing. The pellet green densities were ~3.0 g/cm^3 (65% dense). The pellets were sintered at 1230 ^{o}C (4 h) with a 500 ^{o}C (2 h) binder burnout step. The process yielded uniform pellets with typical density of 4.22 g/cm^3 (91% dense). $HfMgW_3O_{12}$ pellets made in a similar way yielded density of 4.68 g/cm^3 (92% dense).

Figure 4: Photograph of a sintered $Al_{0.5}Sc_{1.5}W_3O_{12}$ pellet.

SEM images of $Al_{0.5}Sc_{1.5}W_3O_{12}$ and $HfMgW_3O_{12}$ cross-sectioned and polished samples are shown in Figure 5 and Figure 6. Extensive microcracking is observed in both samples. Flake-like impurities are observed for the $HfMgW_3O_{12}$ which is likely decomposition during water exposure in polishing. Additional, lower magnification SEM images are shown later in 3.1.2.

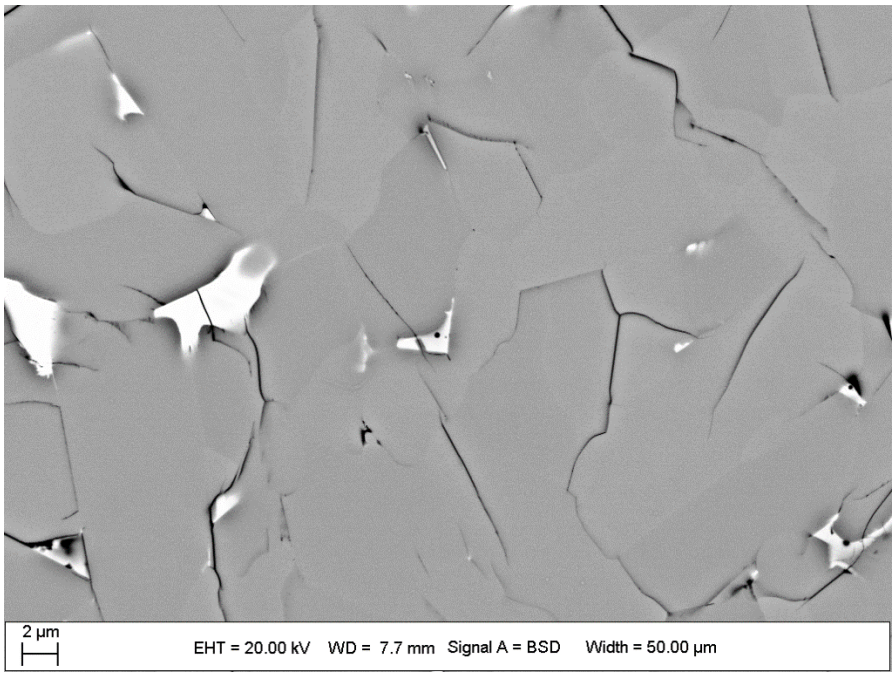

Figure 5: SEM image of sintered $Al_{0.5}Sc_{1.5}W_3O_{12}$

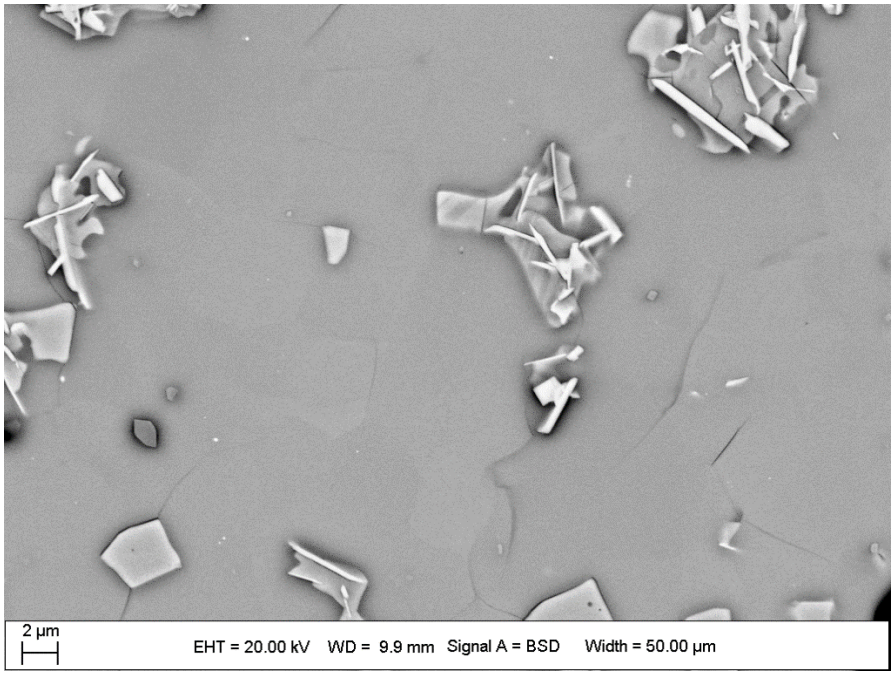

Figure 6: SEM image of sintered $HfMgW_3O_{12}$

3. THERMAL PROPERTIES

3.1. Thermal Expansion

Thermal expansion was measured using dilatometry and/or HTXRD on each of the compositions.

3.1.1. Dilatometry of ZrW_2O_8 and HfW_2O_8

The CTE of ZrW_2O_8 and HfW_2O_8 measured using dilatometry of a dense bulk sample is shown in Figure 7. A Netzsch Dil 402C dilatometer was used. There is a clear negative CTE throughout the temperature range, which becomes very large near the order/disorder transition at ~160 °C, after which CTE stabilizes at ~-5 ppm/°C. The thermal expansion measured here is slightly larger than that reported in the literature, which may be due to impurities in the present material.

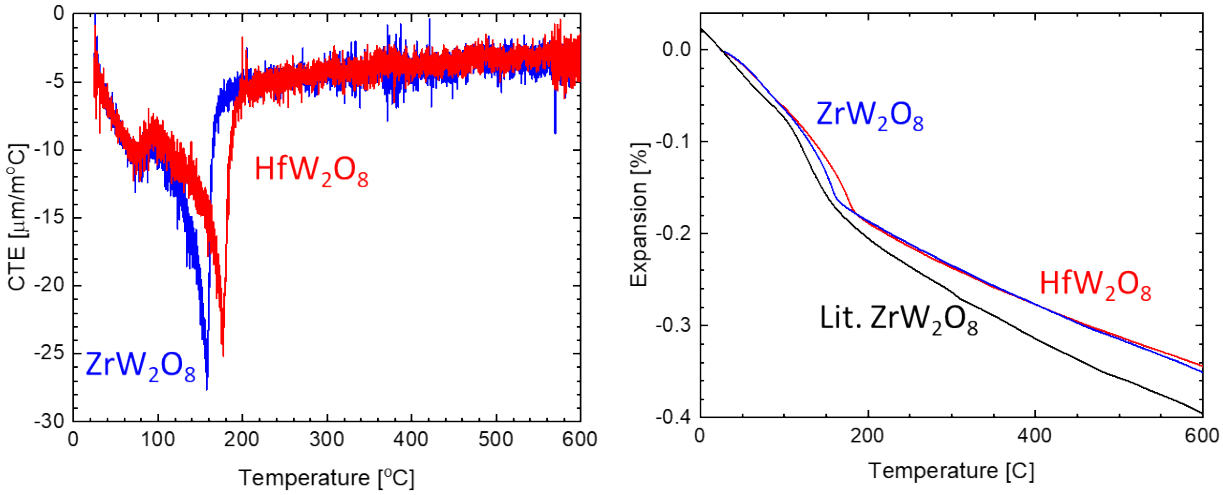

Figure 7: Linear CTE (left) and expansion (right) of ZrW_2O_8 and HfW_2O_8, compared to literature [10].

3.1.2. Dilatometry and thermal cycling of $Al_{0.5}Sc_{1.5}W_3O_{12}$ and $HfMgW_3O_{12}$

The bulk thermal expansion of $Al_{0.5}Sc_{1.5}W_3O_{12}$ and $HfMgW_3O_{12}$ pellets measured using dilatometry is very low, with CTE from a linear fit to the data of 0.57 and 0.76 ppm/°C for $HfMgW_3O_{12}$ and $Al_{0.5}Sc_{1.5}W_3O_{12}$, respectively, as shown in Figure 8. The data was collected for 30 temperature cycles and shows consistent results, indicating that despite the significant anisotropy in this material and micro-cracking, the material can be resilient to thermal cycling within the studied range. Before and after SEM images did not show any obvious change in microstructure or the extent of microcracking, as shown in Figure 9 and Figure 10. A hysteresis is observed in the thermal expansion data, which has been observed previously in the literature and attributed to the anisotropy but not well understood [8]. The expansion of Al_2O_3 ceramic is shown for comparison.

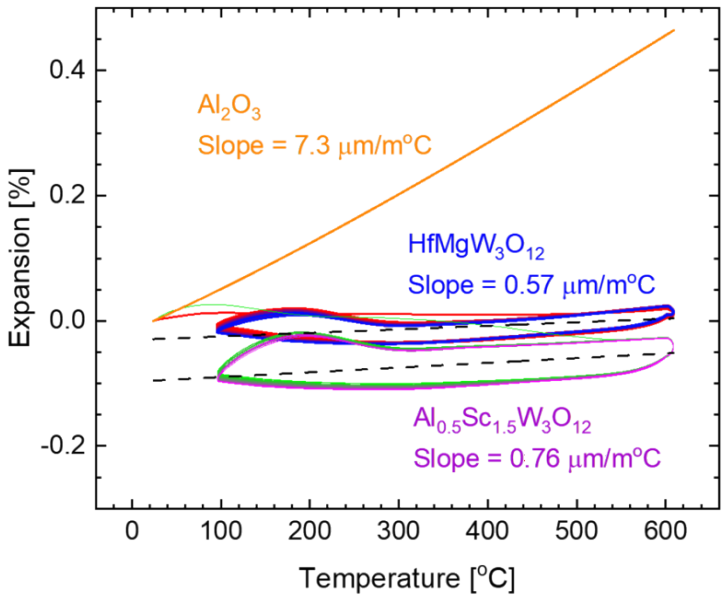

Figure 8: Thermal expansion of $Al_{0.5}Sc_{1.5}W_3O_{12}$ and $HfMgW_3O_{12}$ measured over 30 temperature cycles.

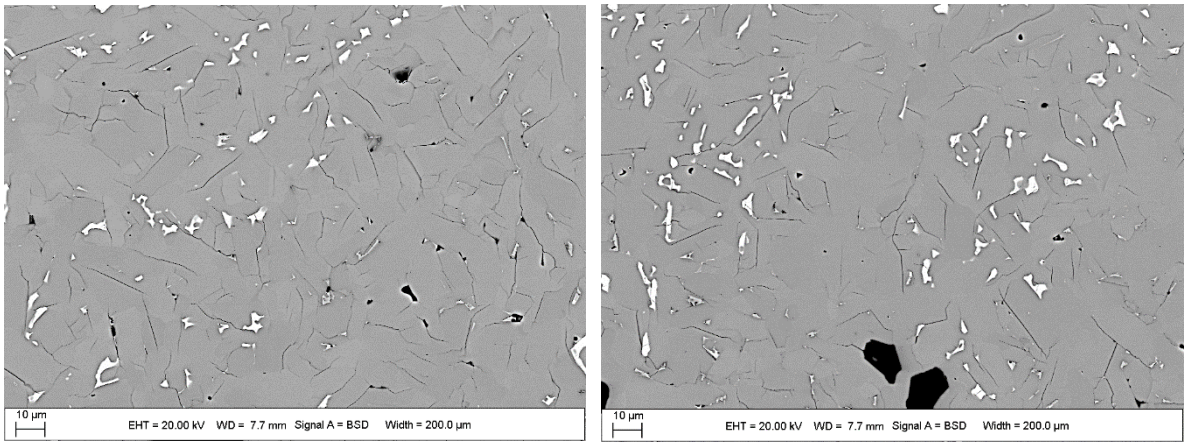

Figure 9: SEM of $Al_{0.5}Sc_{1.5}W_3O_{12}$ before (left) and after (right) thermal cycling shown in Figure 8. Extensive microcracking is observed in both samples, with light regions a possible second phase. Black regions are pores.

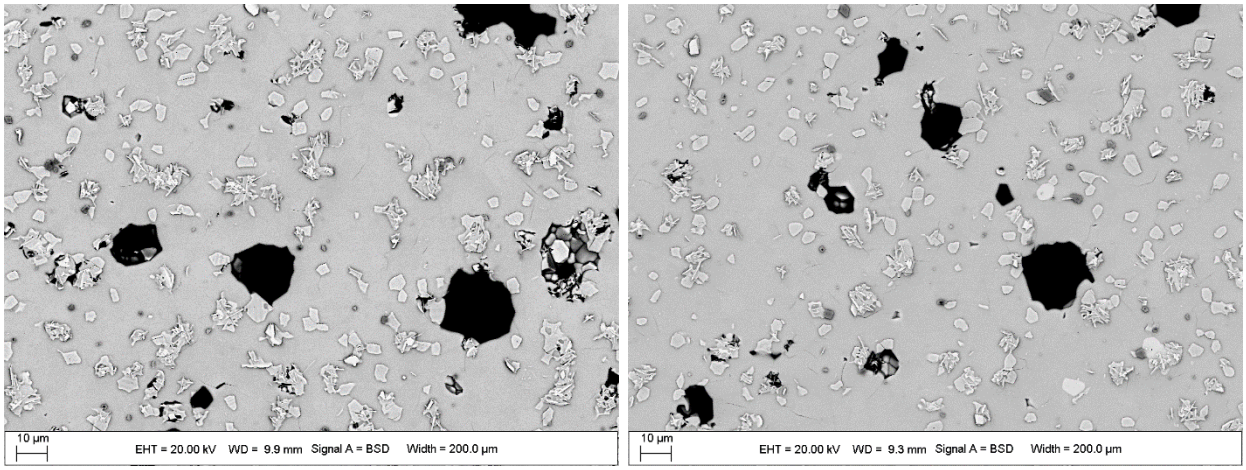

Figure 10: SEM of $HfMgW_3O_{12}$ before (left) and after (right) thermal cycling shown in Figure 8. Faint microcracking is observed, with plate-like particles on surface likely formed during aqueous polishing. Black regions are pores.

3.1.3. HTXRD of $Al_{0.5}Sc_{1.5}W_3O_{12}$, $HfMgW_3O_{12}$, and $Al(HfMg)_{0.5}W_3O_{12}$

$Al_{0.5}Sc_{1.5}W_3O_{12}$, $HfMgW_3O_{12}$, and $Al(HfMg)_{0.5}W_3O_{12}$ lattice parameters and unit cell volumes as a function of temperature were measured using HTXRD in air, as shown in Figure 11, Figure 12, and Figure 13. Error in lattice parameter estimates are shown by the horizontal bars in the figures. HTXRD was done using a Scintag PAD X powder X-ray Diffractometer with CuK_α X-ray source, and incident beam mirror optic, fixed receiving slits and a Peltier-cooled germanium solid-state detector. The ancillary hot-stage was a Buehler HTK 2400 furnace with a Pt/Rh heating strip and surround heater (Edmund Buhler GmbH, Hechingen, Germany).

Similar to dilatometry data, the $Al_{0.5}Sc_{1.5}W_3O_{12}$ and $HfMgW_3O_{12}$ both show a near zero volumetric thermal expansion. Thermal expansion from the linear fits in the plots is reported in Table 3, along with comparison to the literature data. $Al(HfMg)_{0.5}W_3O_{12}$ shows a larger volumetric thermal expansion. Some differences are observed between the present values and those reported in the literature which may be related to slight differences in composition (i.e., different levels of impurity) and/or the temperature range over which CTE was determined (also reported in the table). For the Mg containing compounds, the lattice parameters and unit cell volume show a deviation from the linear temperature behavior observed during cooling which may be related to water absorption by Mg which is released upon heating below ~100 ^oC.

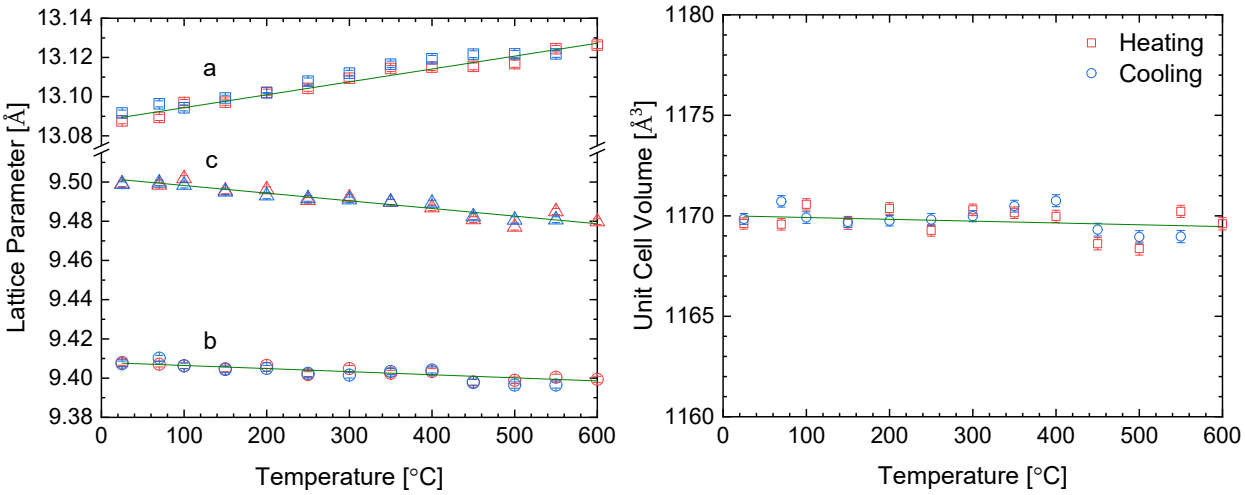

Figure 11: HTXRD derived lattice parameters and unit cell volume for $Al_{0.5}Sc_{1.5}W_3O_{12}$ (red and blue are for heating and cooling, respectively). Straight lines are linear fits to heating data.

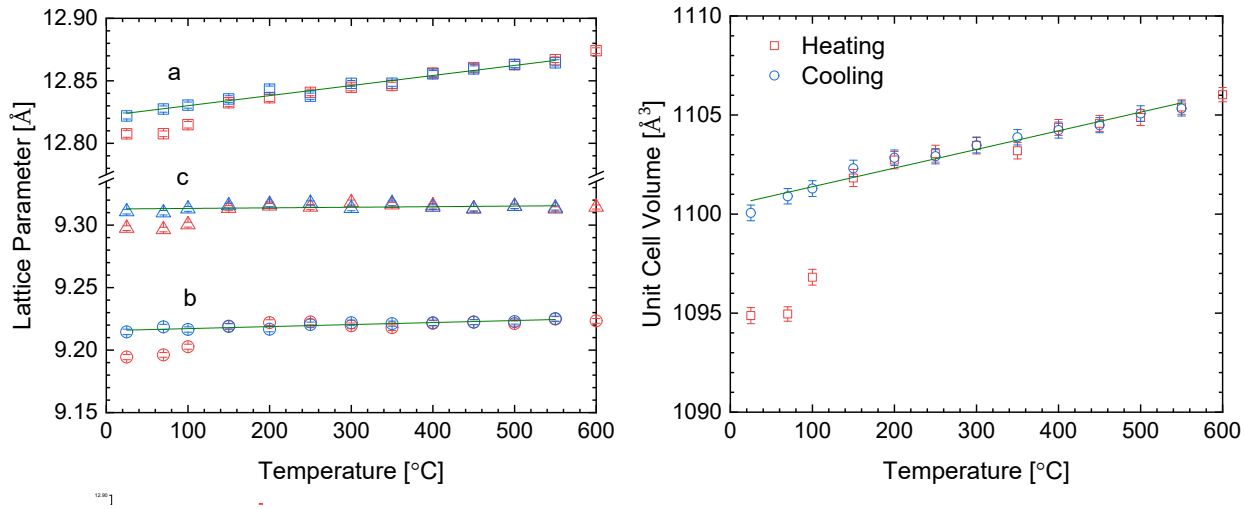

Figure 12: HTXRD derived lattice parameters and unit cell volume for $Al(HfMg)_{0.5}W_3O_{12}$ (red and blue are for heating and cooling, respectively). Straight lines are linear fits to cooling data.

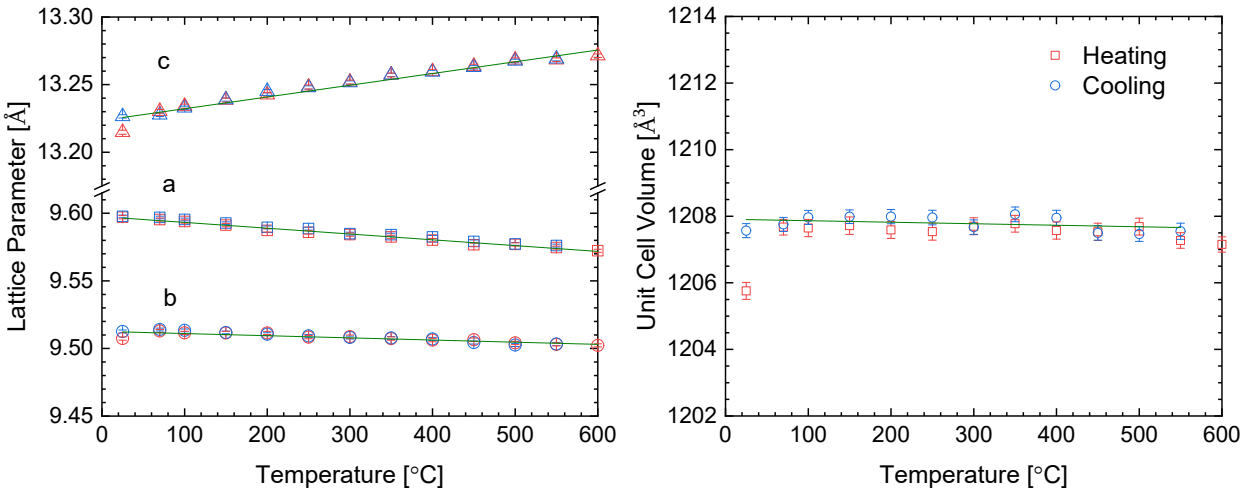

Figure 13: HTXRD derived lattice parameters and unit cell volume for $HfMgW_3O_{12}$ (red and blue are for heating and cooling, respectively). Straight lines are linear fits to cooling data.

Table 3: CTE values for lattice parameters and linear CTE derived from unit cell volume thermal expansion.

Material (Temp. Range)	a [ppm/°C]	b [ppm/°C]	c [ppm/°C]	Linear from Vol. [ppm/°C]
$Al_{0.5}Sc_{1.5}W_3O_{12}$	5.02	-1.68	-4.11	-0.26
$Al_{0.5}Sc_{1.5}W_3O_{12}$ from [7] (-269 °C – 1127 °C)	5.5	-1.9	-3.6	-0.02
$Al(HfMg)_{0.5}W_3O_{12}$	6.28	1.76	0.50	2.85
$Al(HfMg)_{0.5}W_3O_{12}$ from [16] (23 °C – 700 °C)	4.9	0.15	-1.1	1.32
$HfMgW_3O_{12}$	6.56	-1.68	-4.47	-0.13
$HfMgW_3O_{12}$ from [16] (23 °C – 700 °C)	5.26	-2.33	-5.24	-0.77

3.2. Thermal and atmosphere stability

The thermal stability of ZrW_2O_8 and HfW_2O_8 are already well documented [4]. The thermal stability of $Al_{0.5}Sc_{1.5}W_3O_{12}$ is less well known so DTA was measured in air at high temperature and is shown in Figure 14. Netzsch STA449 F1 or F3 were used for TGA. $Al_{0.5}Sc_{1.5}W_3O_{12}$ on the first heating shows a dip at 1250 °C which may be an instrumental artifact (it is also observed on the first run for the other material shown), it is also worth noting the material had previously been sintered at 1230 °C. However, on the second heat (without removing the sample from the instrument), there are no peaks indicating a phase transition, suggesting the material is phase stable up to at least the maximum testing temperature of 1350 °C. Additionally, the measurement was performed in an alumina crucible, indicating stability towards reactivity with alumina (unlike most of the other tungstates examined here). Another material fabricated in this project, $Al(HfMg)_{0.5}W_3O_{12}$ in contrast

shows a reproducible peak at ~1160 °C consistent with melting or reaction with the alumina crucible (with post-test observation of the crucible and sample supporting either or both scenarios).

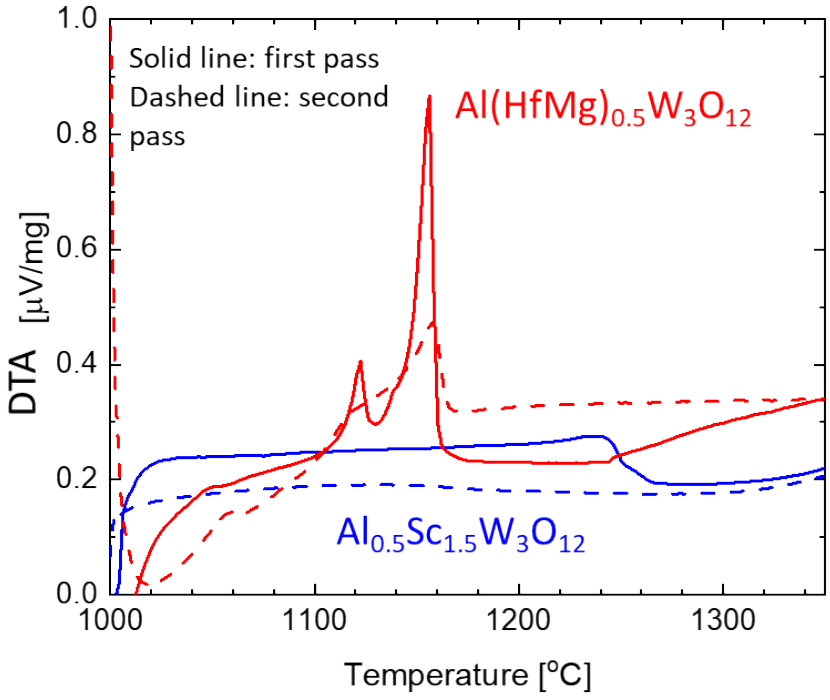

Figure 14: DTA showing melting of $Al(HfMg)_{0.5}W_3O_{12}$ at ~1160 °C as compared to $Al_{0.5}Sc_{1.5}W_3O_{12}$ which does not exhibit an obvious phase change up to the maximum measurement temperature.

TGA analysis was also performed on the $Al_{0.5}Sc_{1.5}W_3O_{12}$ in N_2 to examine the impact of exposure to reducing/inert gas atmospheres. There is an initial mass loss at ~350 °C which may be related to loss of adsorbed species (such as water or CO_2), followed by a stable mass until ~1300 °C where significant mass loss occurs. The high temperature mass loss is an indication of reduction, and possibly may lead to decomposition of the material. Therefore, the material may not be stable above ~1300 °C in inert/reducing conditions. As shown later in the section on brazing, the $Al_{0.5}Sc_{1.5}W_3O_{12}$ also displays apparent phase stability in high vacuum up to 980 °C.

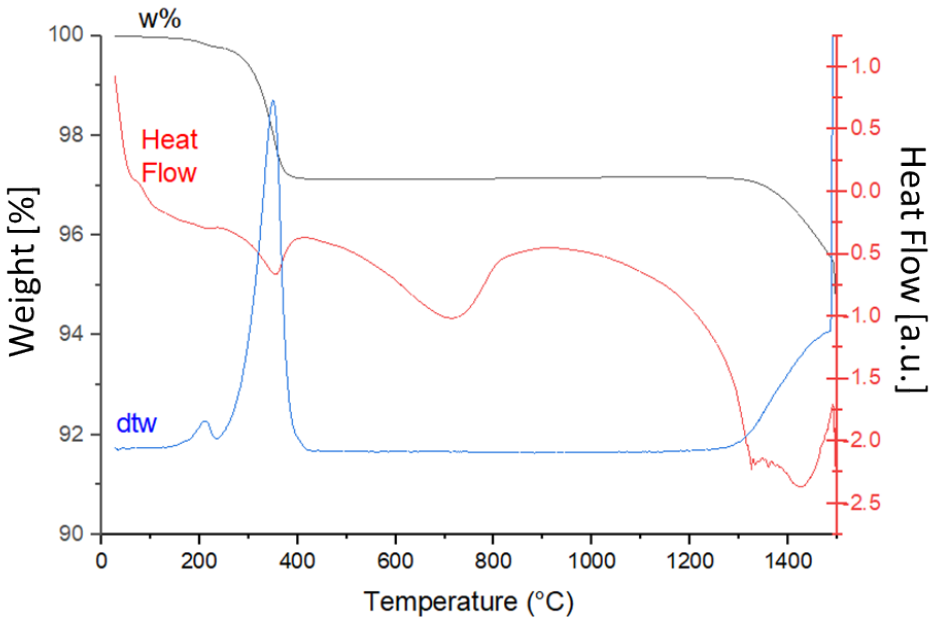

Figure 15: TGA of $Al_{0.5}Sc_{1.5}W_3O_{12}$ measured in N_2, showing weight change (black), heat flow (red), and a differential weight change (blue).

The thermal stability in inert conditions of ZrW_2O_8, HfW_2O_8 and $HfMgW_3O_{12}$ were also examined. There were slight color changes after 700 °C annealing, and significantly more grey coloration formation after annealing at 1100 °C (only the $HfMgW_3O_{12}$ sample annealed at this latter condition), as shown in Figure 16. The oxygen partial pressure was estimated to be ~10^{-3} atm O_2 from an oxygen sensor reading, which is much larger than expected and may be related to significant leaking in the tube. No samples exhibited a phase change after the 700 °C anneal, however, the $HfMgW_3O_{12}$ showed extensive decomposition after annealing at 1100 °C into HfO_2, WO_2, and $MgWO_4$ phases, as shown in Figure 17.

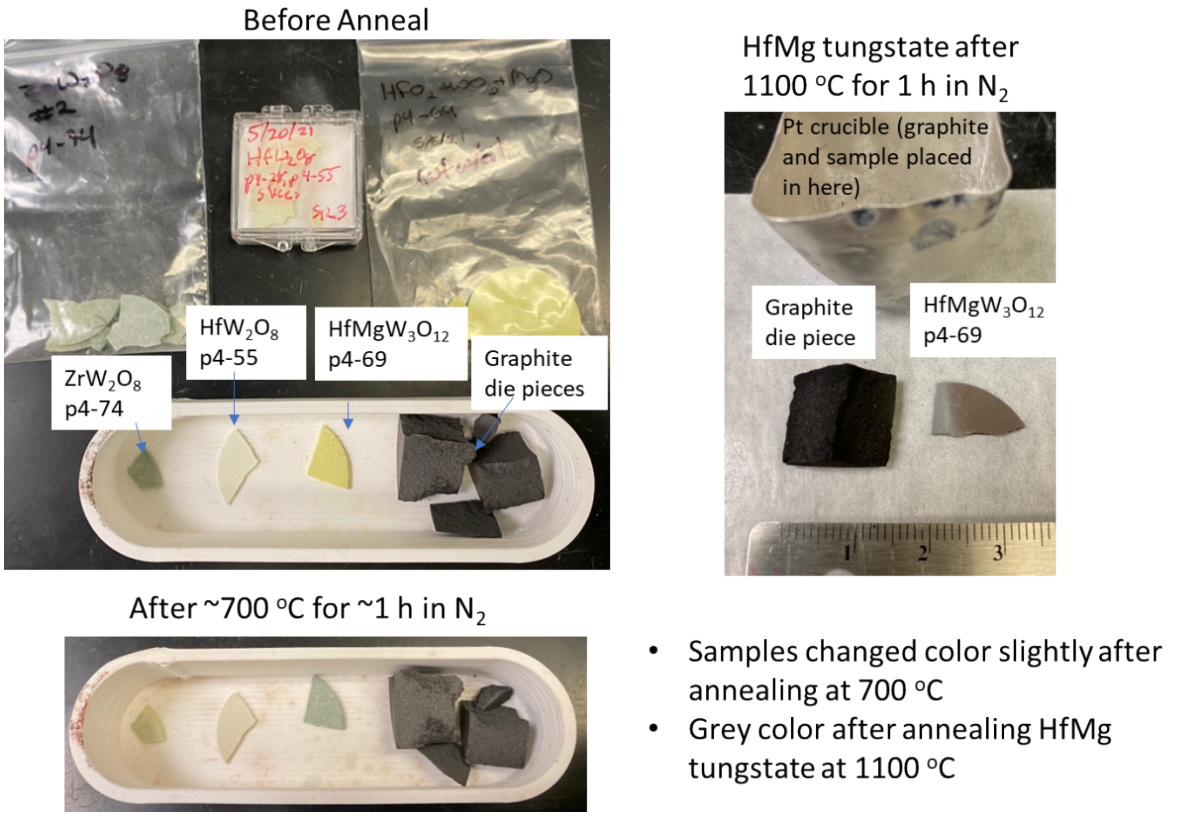

Figure 16: Sample color changes after annealing ZrW_2O_8, HfW_2O_8 and $HfMgW_3O_{12}$ in N_2 at 700 °C and 1100 °C.

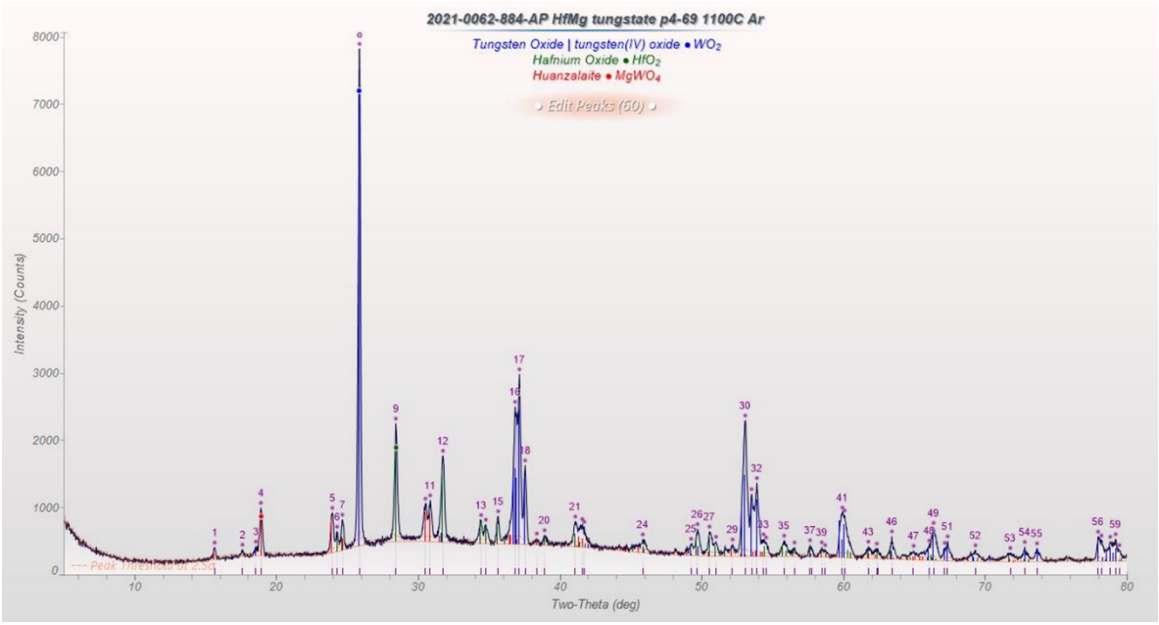

Figure 17: XRD pattern for $HfMgW_3O_{12}$ after 1100 °C anneal in N_2.

3.3. Heat capacity of ZrW_2O_8, $Al_{0.5}Sc_{1.5}W_3O_{12}$, and $HfMgW_3O_{12}$

Constant pressure heat capacity (C_p) of ZrW_2O_8, $Al_{0.5}Sc_{1.5}W_3O_{12}$, and $HfMgW_3O_{12}$ were measured using A Netzsch DSC 214 in Ar gas. ZrW_2O_8 shows the expected general increase in C_p with increasing temperature, however, there is a spike in C_p at ~160 °C corresponding to the order-disorder phase transition, as shown in Figure 18. Since the low thermal conductivity of tungstates can impact thermal equilibration in DSC measurements, two different masses were examined to ensure reproducibility [17]. For the ZrW_2O_8, the two samples show similar results across the measurement range reported.

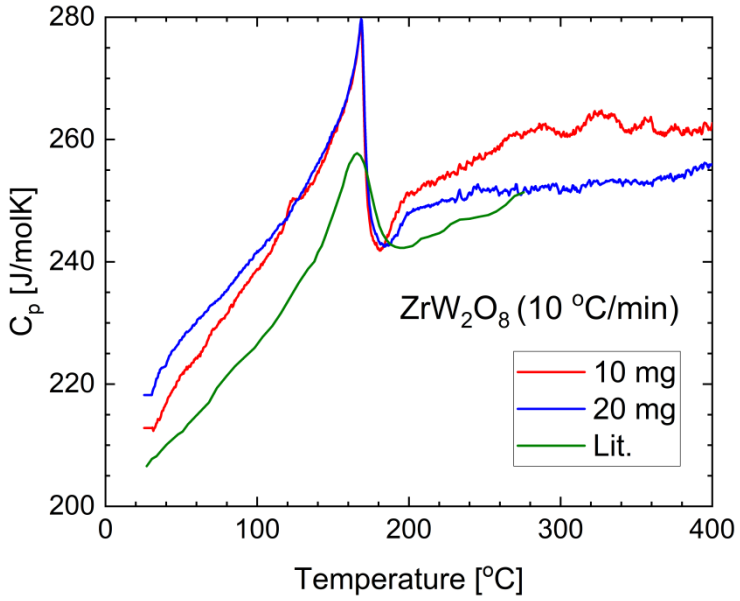

Figure 18: Heat capacity measured for ZrW_2O_8 and compared with literature (green) from [18]. The ramp rate for DSC is reported in the figure.

C_p was measured for multiple samples and masses using different sapphire reference masses for $Al_{0.5}Sc_{1.5}W_3O_{12}$ and is reported in Figure 19. Significant variation across the datasets was observed and described below. Poor thermal equilibration from low thermal conductivity described above, is observed to erroneously decrease C_p at high temperatures for both the 10 and 20 mg samples (with sapphire disk reference), with a greater deviation observed for the larger sample mass, as expected. For measurements starting at room temperature (sample A and sample B), there is an erroneous drop in C_p related to initial thermal equilibration of the system, which is removed when measurements are started at 0 °C, as shown by the other measurements in the figure.

It is suggested that measurement accuracy is improved by matching the measured heat flux of the reference to the sample. At room temperature, C_p for the sapphire reference is ~0.8 J/gK and is expected to be ~0.3 J/gK for the $Al_{0.5}Sc_{1.5}W_3O_{12}$, meaning for 10 mg of tungstate, ~3-4 mg of sapphire reference is needed for the heat flux match. As shown in Figure 19, decreasing the reference mass significantly decreased the reported C_p, by as much as 38%. It is worth noting that the reference morphology was changed from a dense sapphire disk to a powder (as indicated in the

graph legend), though comparisons of the disk and an equivalent mass of powder showed up to ~10% variation in heat flux, meaning the total variability of the tungstate data is not likely solely due to the type of reference. A likely significant source of error is that the heat flux being measured is ~10% of the heat flux expected of the Al sample container (~38 mg, ~0.9 J/gK at room temp.). Smaller amounts of reference material are likely resulting in greater errors in the correction data. This is further evident in the large C_p of ~500 J/molK measured at 550 °C which is significantly greater than the approximate maximum of 424 J/molK estimated from the Dulong-Petit law[1], with no evidence of the expected non-thermal equilibrium drop.

Given the above discussion, the "10 mg sample C 12 mg sapph. disk" curve (green line) up to ~300 °C is believed to be the most reliable result. This yields a room temperature C_p estimate of ~260 J/molK for $Al_{0.5}Sc_{1.5}W_3O_{12}$.

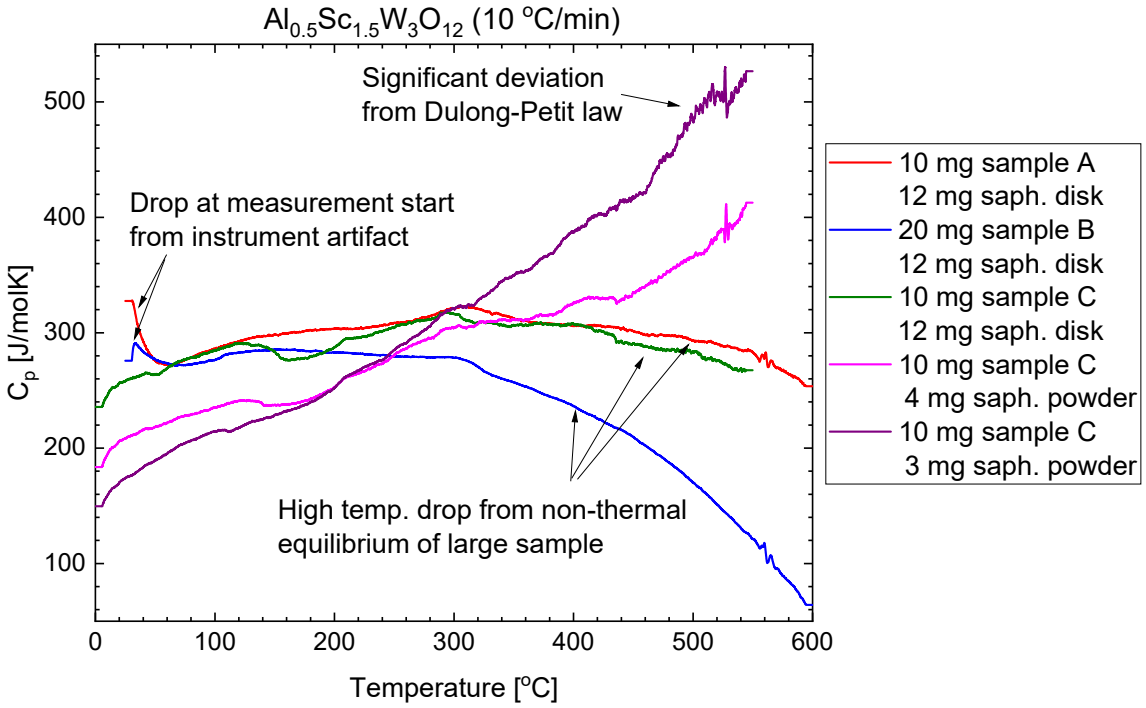

Figure 19: Heat capacity of $Al_{0.5}Sc_{1.5}W_3O_{12}$. Ramp rate is reported in the figure.

C_p measured for $HfMgW_3O_{12}$ is shown in Figure 20. ~15-20% variation in the measurement data is observed near room temperature. A less thorough examination of error sources was performed for this data, and thus the average of the results (estimating a subtraction of the low temperature measurement artifact) was used, resulting in a room temperature C_p estimate of ~280 J/molK for $HfMgW_3O_{12}$. For comparison, C_p for $HfMgMo_3O_{12}$ has been reported to be ~300 J/molK at room temperature [20], very similar to the present tungstate version. C_p for $HfMo_2O_8$ at room temperature

[1] Note that the Dulong-Petit law (i.e., $C_v = 3nR$) is for constant volume heat capacity (C_v). C_p (measured here) is larger than C_v by α^2BVT ([19] Zhang, J., et al., *Journal of Applied Physics*, 114 (17) p. 173509 (2013).). However, since α is near zero here and thus C_p, even at elevated temperatures, is not expected to be much larger than C_v.

is reported to be ~200 J/molK [17], which is also similar to ZrW_2O_8 shown in Figure 18, indicating the tungstate and molybdate versions have similar C_p.

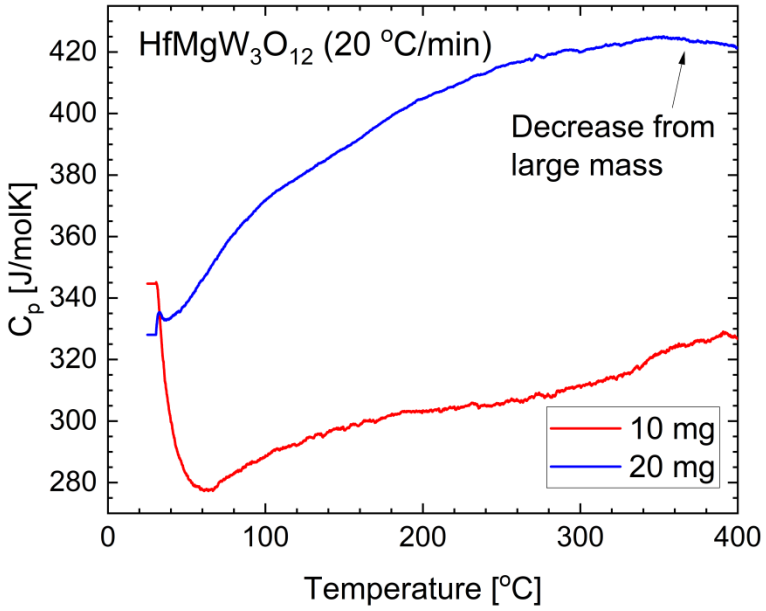

Figure 20: Heat capacity of $HfMgW_3O_{12}$. Ramp rate is reported in the figure.

3.4. Thermal diffusivity and conductivity of $Al_{0.5}Sc_{1.5}W_3O_{12}$ and $HfMgW_3O_{12}$

Thermal diffusivity of $Al_{0.5}Sc_{1.5}W_3O_{12}$ and $HfMgW_3O_{12}$ were measured in this project using a Netzsch LFA 467. Approximately 1 sq. cm samples were used, with two different thickness to confirm reproducibility and bulk measurement (as opposed to a surface effect). The thermal diffusivity for $Al_{0.5}Sc_{1.5}W_3O_{12}$ and $HfMgW_3O_{12}$ are shown in Figure 21 and Figure 22, respectively. Thermal conductivity (κ) is calculated from thermal diffusivity (α_T) using the following equation.

$$\kappa = \alpha_T \rho C_p$$

Using α_T of 0.36 mm^2/s, ρ of 4.35 g/cm^3, and C_p of 260 J/molK (0.32 J/gK) for $Al_{0.5}Sc_{1.5}W_3O_{12}$ yields a room temperature κ of 0.50 W/mK. Using α_T of 0.40 mm^2/s, ρ of 4.68 g/cm^3, and C_p of 280 J/molK (0.30 J/gK) for $HfMgW_3O_{12}$ yields a room temperature κ of 0.56 W/mK. For comparison, κ is reported in the literature for $HfMgMo_3O_{12}$ to be ~1 W/Km [20], for ZrW_2O_8 it is ~0.78 W/mK [18], and for $HfMo_2O_8$ it is 0.64 W/mK [17]. The values reported here for $Al_{0.5}Sc_{1.5}W_3O_{12}$ and $HfMgW_3O_{12}$ are of similar magnitude to these other tungstates. It is worth noting κ of the tungstates is very low, for example, κ at room temperature for ZrO_2 is ~3 W/mK, for sapphire (i.e., Al_2O_3) it is ~40 W/mK [21], and for metals it is typically >100 W/mK.

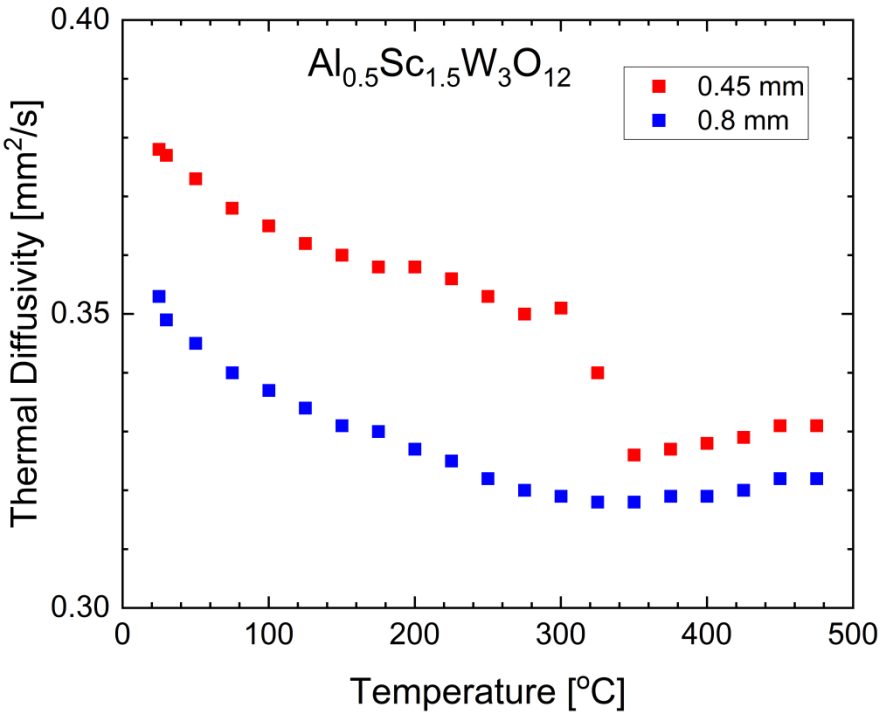

Figure 21: Thermal diffusivity of $Al_{0.5}Sc_{1.5}W_3O_{12}$ for two sample thicknesses.

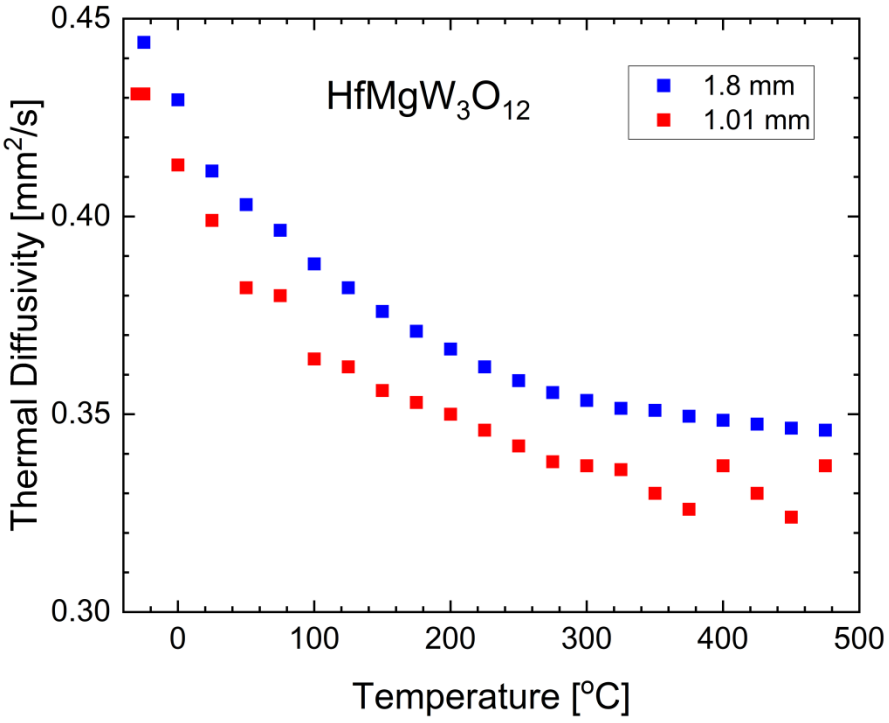

Figure 22: Thermal diffusivity of $HfMgW_3O_{12}$ for two sample thicknesses.

3.5. Elastic properties of HfW_2O_8, $Al_{0.5}Sc_{1.5}W_3O_{12}$, and $HfMgW_3O_{12}$

The elastic properties of HfW_2O_8, $Al_{0.5}Sc_{1.5}W_3O_{12}$, and $HfMgW_3O_{12}$ were determined and reported in Table 4, where B is bulk modulus, E is elastic modulus, G is shear modulus, and ν is Poisson's ratio. The bulk modulus values are low in comparison with typical values for ceramics (~>100 GPa), but are comparable to the 48 GPa reported in the literature for ZrW_2O_8 (measured using pulse-echo) [14]. The $Al_{0.5}Sc_{1.5}W_3O_{12}$ sample was only 1.76 mm thick and ~2 cm diameter and was measured using a pulse-echo system. The HfW_2O_8 and $HfMgW_3O_{12}$ were measured using resonant ultrasound spectroscopy (RUS) and were 7.1 and 3.1 cm thick, respectively, and about 2 cm in diameter. Except for the HfW_2O_8, the densities are high. The elastic moduli for $Al_{0.5}Sc_{1.5}W_3O_{12}$ and $HfMgW_3O_{12}$ are lower than for HfW_2O_8, which may either be related to the difference in crystal structure between these materials, or more likely the significant amount of micro-cracking in the former, anisotropic materials.

Table 4: Elastic properties measured for selected tungstates

Material	B [GPa]	E [GPa]	G [GPa]	ν	ρ [g/cm^3]	$\rho/\rho_{Theor.}$
HfW_2O_8	32	51	21	0.23	4.98	85%
$Al_{0.5}Sc_{1.5}W_3O_{12}$	34	37	14	0.32	4.35	94%
$HfMgW_3O_{12}$	16	33	14	0.15	5.08	98%

3.6. Grüneisen parameter estimate for $Al_{0.5}Sc_{1.5}W_3O_{12}$ and $HfMgW_3O_{12}$

The Grüneisen parameter (γ) is defined by the following equation:

$$\gamma = \frac{\alpha B V}{C_v}$$

where α is the volumetric thermal expansion coefficient (~3 x linear CTE (from Figure 8)), C_v is the heat capacity at constant volume, and V is molar volume (from ρ_{Theor} in Table 2). $C_v = C_p - \alpha^2 BVT$ [19], and since α is near zero here, $C_v \sim C_p$. From values reported here, γ is estimated at room temperature for $Al_{0.5}Sc_{1.5}W_3O_{12}$ and $HfMgW_3O_{12}$ are 0.05 and 0.02, respectively. Since the bulk CTE is so close to zero for both these materials, γ is also very close to 0. In comparison, γ ~-0.8 for ZrW_2O_8 [14] and typically ~1-2 for most other materials.

4. INTEGRATION OF $Al_{0.5}SC_{1.5}W_3O_{12}$ WITH OTHER MATERIALS

$Al_{0.5}Sc_{1.5}W_3O_{12}$ was fabricated in different forms to examine methods for integrating it with other materials. As described below, this included dispersing the tungstate powder with epoxy and casting it with a commercial supplier, dispersing the powder in epoxy at Sandia and casting it on stainless steel, dispersing the powder in glass and annealing it on stainless steel, and brazing bulk pellets to Invar or tungsten. Dispersion of powder in epoxy worked well, and such a solution could be diluted to enable spraying of the mixture. However, the limited operating temperature range of the epoxy could pose challenges in some applications. Also note the epoxies used here are not optimized for limited thermal expansion.

4.1. Dispersion in epoxy with TPL

$Al_{0.5}Sc_{1.5}W_3O_{12}$ was dispersed in a flexible polymer matrix through a collaboration with TPL, Inc. in Albuquerque, NM. Epoxy composition and process development was largely performed in another project [22]. 50 vol% of the tungstate was mixed by TPL with TPL epoxy and cured as either a single layer, or in a bilayer on a previously fabricated 50 vol% $ZnFe_2O_4$ powder in TPL epoxy, as shown in Figure 23. The individual layers could not be readily separated in the bilayer, indicating good adhesion.

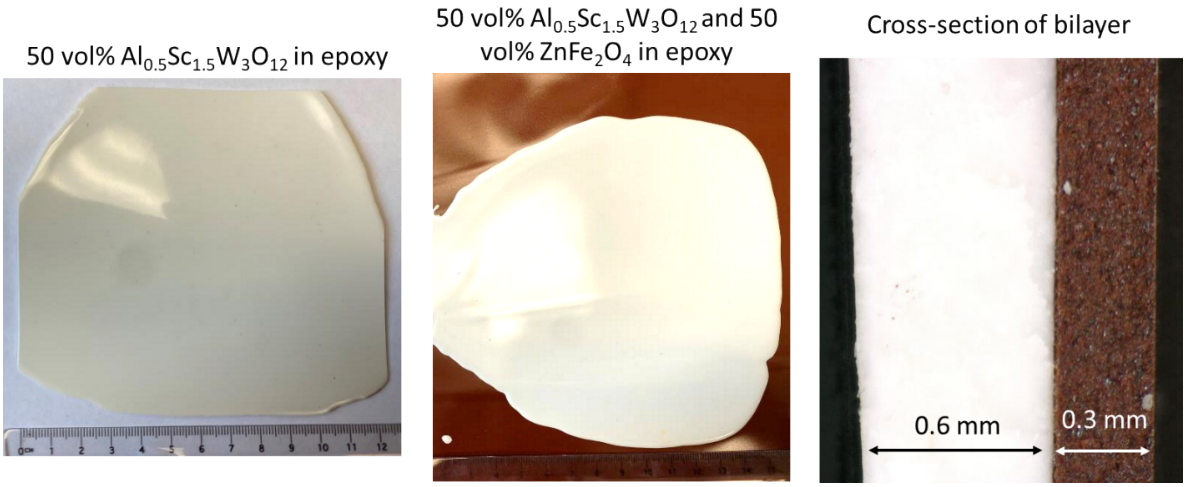

Figure 23: $Al_{0.5}Sc_{1.5}W_3O_{12}$ in flexible epoxy single layer (left), deposited on a sheet of $ZnFe_2O_4$ in flexible epoxy to make a bilayer (center), and optical cross-section of bilayer (right).

The mass loss of the TPL epoxy with $Al_{0.5}Sc_{1.5}W_3O_{12}$ upon heating in air measured using TGA is shown in Figure 24. At ~250 °C mass starts to decrease indicating that may be the maximum use temperature of the material.

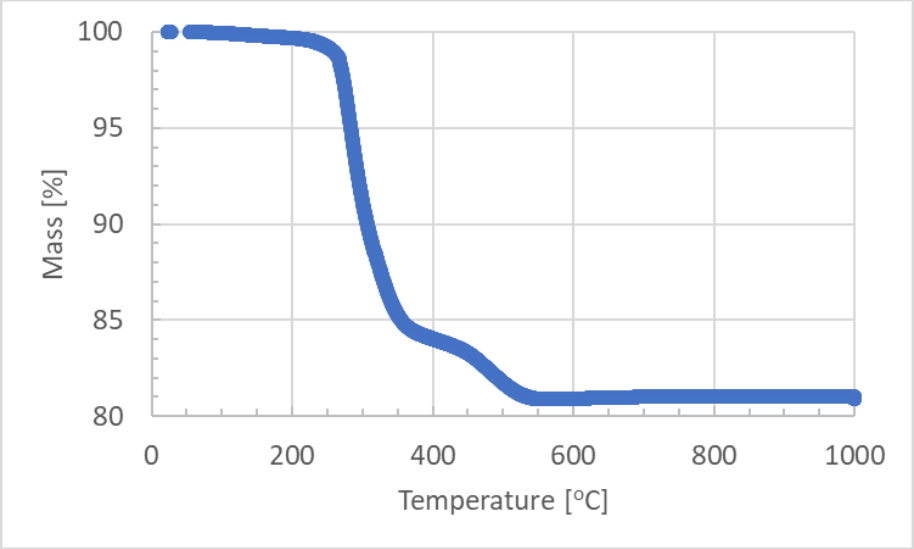

Figure 24: Mass change of $Al_{0.5}Sc_{1.5}W_3O_{12}$ in epoxy

4.2. Dispersion in epoxy on stainless steel

An $Al_{0.5}Sc_{1.5}W_3O_{12}$ powder embedded in epoxy and applied to stainless steel was explored. An epoxy using Epon 828 with Epikure 3072 curing agent was used. Epikure 3072 can be used to make a metal adhesive. 30 vol% of tungstate powder was mixed with Epon and Epikure first by hand and then in a Thinky mixer. Epon:Epikure was 1.3:0.46 by weight. The mixture was spread on a disk of SS316 and cured at 100 °C for 24 h. The final component is shown in Figure 25. The coating appears rough and can be removed by prying it off with a razor blade. The roughness can be addressed by thinning the mixture prior to coating (e.g., by addition of solvent). The poor adhesion may be mitigated by roughening the SS316 disk, improved cleaning (beyond the ultrasonication in isopropanol performed here) and/or by exploring alternative epoxy adhesives.

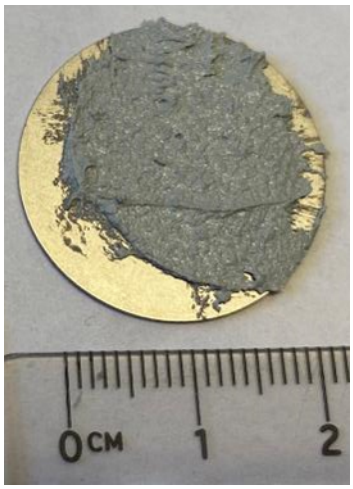

Figure 25: Mixture of $Al_{0.5}Sc_{1.5}W_3O_{12}$ in Epikure epoxy adhered to a disk of SS316

4.3. Dispersion in glass

$Al_{0.5}Sc_{1.5}W_3O_{12}$ powder was also mixed with glass powder with polyvinyl butyral (PVB) binder with ethanol. Glass is expected to provide a higher temperature resistance than the flexible polymer described above. ~0.78 g of glass, 0.3 g PVB (previously dissolved in ethanol), and 11.14 g of tungstate were mixed using a Thinky mixer. The glass used was Corning 7572 powder. The slurry was painted on to a SS316 substrate and annealed at 450 °C for 1 h in air. The annealed mixture easily slid off of the substrate and unfortunately was lost.

4.4. Brazing

Four brazing attempts were made, the first three with progressively increasing temperatures and the fourth with a different substrate. Only the last two are discussed, and in both cases, brazing was not successful in joining $Al_{0.5}Sc_{1.5}W_3O_{12}$ with the substrate.

Invar and tungsten substrates were used. Invar has a very low thermal expansion which rises above ~200 °C, reaching ~14 ppm/°C at 900 °C, in the range of the brazing temperature. To aid in avoiding CTE mismatch between the tungstate and the substrate, a tungsten substrate was examined with CTE ~4.5 ppm/°C.

Brazing was performed in a vacuum furnace by heating the sample at 15 °C/min to the preheat temperature, holding for 15 min, and then heating at 10 °C/min to the brazing temperature and holding for 10 minutes. Acetone and alcohol were used to clean substrates and the braze alloy foil. 0.002 in. thick braze foil was used with the metal substrate placed at the bottom, with foil between the tungstate sample and substrate and a weight on top of the tungstate. Vacuum pressure was ~10^{-5} Torr.

Ag-Cu-Zr (97Ag-1Cu-2Zr) braze was used with a preheat temperature of 900 °C and a braze temperature of 980 °C. The alloy showed good wetting to the Invar substrate with some evidence of possible tearout of the tungstate pellet, as shown in Figure 26. The tungstate pellet exhibits significant darkening from the original lime-green color indicative of reduction in the high temperature low oxygen pressure brazing atmosphere. Despite the discoloration, no secondary phases were obviously detected in XRD, as shown in Figure 27, and is in general agreement with the stability shown in reducing anneals in the previous section on thermal stability of tungstates. The poor adhesion of the sample to the braze may be from a large CTE mismatch with the tungstate fracturing at the braze interface.

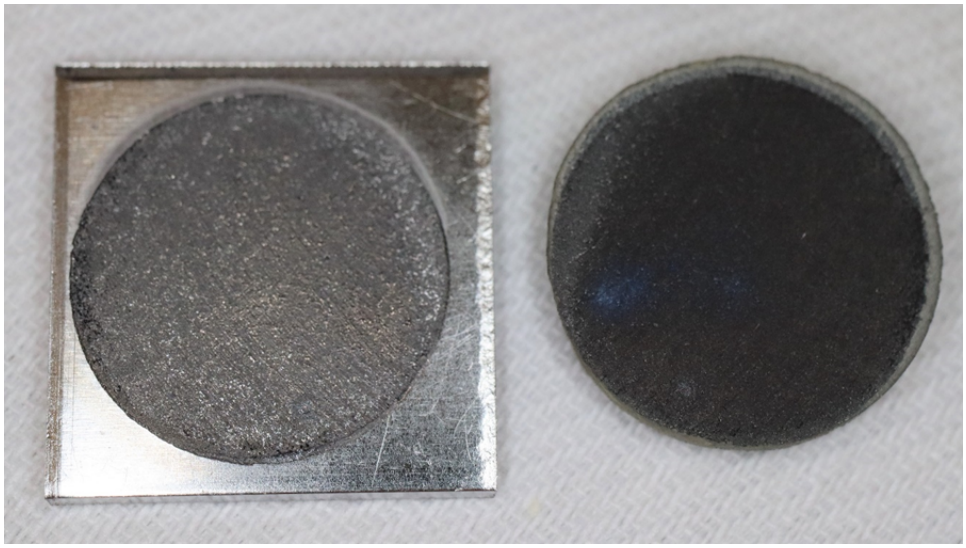

Figure 26: Invar substrate with well-wetting braze layer showing roughness where sample had been sitting (left). Side of sample in contact with braze not showing any evidence of braze wetting and also severe darkening (right).

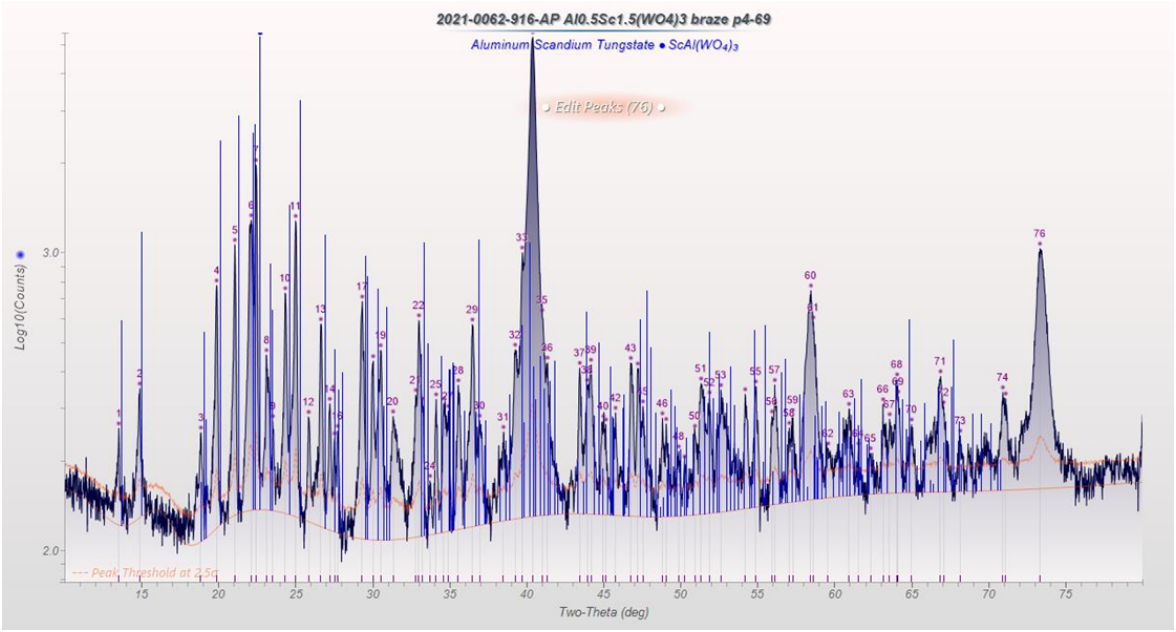

Figure 27: XRD of $Al_{0.5}Sc_{1.5}W_3O_{12}$ pellet after brazing operation with Invar.

A tungsten substrate was also examined using the same braze and annealing conditions that were used for the Invar substrate. As in the previous case, the $Al_{0.5}W_3O_{12}$ sample did not adhere to the substrate, though there was evidence of some bonding/tearout of the tungstate, particularly near the outer diameter of braze, as shown in Figure 28.

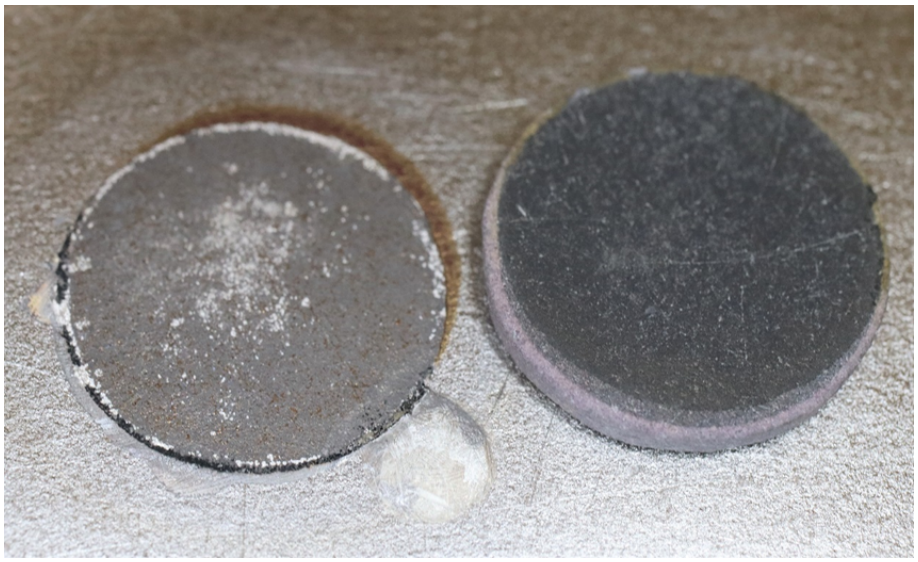

Figure 28: Braze on tungsten substrate (left) and $Al_{0.5}Sc_{1.5}W_3O_{12}$ face in contact with braze (right). There is some evidence of tungstate bonding to braze at outer diameter of braze.

The Zr active braze alloy showed evidence of bonding to the tungstate. Ti active braze alloys (which have a lower brazing temperature) explored in earlier braze operations (not shown here) did not appear to react (i.e., bond) with the tungstate. The large CTE mismatch between the tungstate and substrate and high temperature needed for brazing likely lead to the non-successful brazing. The tungstate may also have poor mechanical strength.

5. SUMMARY

ZrW_2O_8, HfW_2O_8, $HfMgW_3O_{12}$, $Al(HfMg)_{0.5}W_3O_{12}$, and $Al_{0.5}Sc_{1.5}W_3O_{12}$ were fabricated and thermal expansion were analyzed. The cubic tungstates (ZrW_2O_8 and HfW_2O_8) were shown to have negative CTE consistent with literature, with a very large value near the order/disorder transition at ~160 – 180 °C. The non-cubic, anisotropic tungstates ($HfMgW_3O_{12}$, $Al(HfMg)_{0.5}W_3O_{12}$, and $Al_{0.5}Sc_{1.5}W_3O_{12}$) were shown to have CTE much closer to zero, as expected and consistent with the literature. $Al_{0.5}Sc_{1.5}W_3O_{12}$ was found to have much better thermal stability than the other cubic or non-cubic tungstates both in air and inert (N_2) environments up to 1300 °C. Due to the near zero CTE, bulk Gruneisen parameter of $Al_{0.5}Sc_{1.5}W_3O_{12}$ and $HfMgW_3O_{12}$ are very low at 0.05 and 0.02, respectively. Thermal conductivity was also found to be very low for $Al_{0.5}Sc_{1.5}W_3O_{12}$ and $HfMgW_3O_{12}$ at 0.50 W/mK and 0.56 W/mK, respectively, and in general agreement with values reported for other tungstates and molybdates.

Methods to integrate the $Al_{0.5}Sc_{1.5}W_3O_{12}$ with other materials were investigated, including brazing ceramic pellets to low CTE metals and embedding the ceramic powder in flexible epoxy, or epoxy or glass adhered to a SS316 substrate. Brazing proved unsuccessful. Embedding ceramic powder at 50 vol% solids loading in flexible epoxy was demonstrated.

Lastly, processing challenges for the cubic tungstates were discussed (i.e., obtaining single phase for large scale quenching operations). $Al_{0.5}Sc_{1.5}W_3O_{12}$ was relatively simple to fabricate, and more than 1 kg was made in the project.

REFERENCES

[1] Sleight, A.W., *Annual Review of Materials Science*, 28 (1) p. 29-43 (1998).
[2] Lind, C., *Materials*, 5 (6) p. 1125-1154 (2012).
[3] Evans, J.S.O., et al., *Chemistry of Materials*, 8 (12) p. 2809-2823 (1996).
[4] Chang, L.L.Y., M.G. Scroger, and B. Phillips, *Journal of the American Ceramic Society*, 50 (4) p. 211-215 (1967).
[5] Kanamori, K., et al., *Journal of the American Ceramic Society*, 91 (11) p. 3542-3545 (2008).
[6] Li, F., et al., *Journal of Solid State Chemistry*, 218 (15-22 (2014).
[7] Liu, J., et al., *Chemistry of Materials*, 33 (10) p. 3823-3831 (2021).
[8] Niladri, D., et al. *Synthesis, characterization, and densification of $Al_{2-x}Sc_x(WO_4)_3$ ceramics for low-expansion infrared-transparent windows*. in *Proc.SPIE*. 2011.
[9] Nassau, K., H.J. Levinstein, and G.M. Loiacono, *Journal of Physics and Chemistry of Solids*, 26 (12) p. 1805-1816 (1965).
[10] Evans, A.G., *Acta Metallurgica*, 26 (12) p. 1845-1853 (1978).
[11] *PDF 01-082-8412*.
[12] *PDF 00-060-0843*.
[13] *Refined from PDF 01-078-2841*.
[14] Ernst, G., et al., *Nature*, 396 (6707) p. 147-149 (1998).
[15] Bishop, S.R., *Dynamic high pressure phase transformation of ZrW_2O_8*. In preparation.
[16] Suzuki, T. and A. Omote, *Journal of the American Ceramic Society*, 89 (2) p. 691-693 (2006).
[17] Kennedy, C.A., et al., *Physical Review B*, 75 (22) p. 224302 (2007).
[18] Hashimoto, T., et al., *Solid State Communications*, 131 (3) p. 217-221 (2004).
[19] Zhang, J., et al., *Journal of Applied Physics*, 114 (17) p. 173509 (2013).
[20] Miller, K.J., et al., *Solid State Communications*, 152 (18) p. 1748-1752 (2012).
[21] Burghartz, S. and B. Schulz, *Journal of Nuclear Materials*, 212-215 p. 1065-1068 (1994).
[22] San Martin, L., et al., *Development and Use of EM Resonance Dampeners to Improve Cavity Shielding Effectiveness and Circuit Operation*. SAND In review.

APPENDIX A. PARTICLE SIZE

This section describes initial particle size and impact of milling for several examples. Powder sources are provided in Table 1.

A.1. Initial particle size

Starting particle sizes for ZrO_2, WO_3, MgO, HfO_2, Al_2O_3, and Sc_2O_3 are shown in the figures of this section.

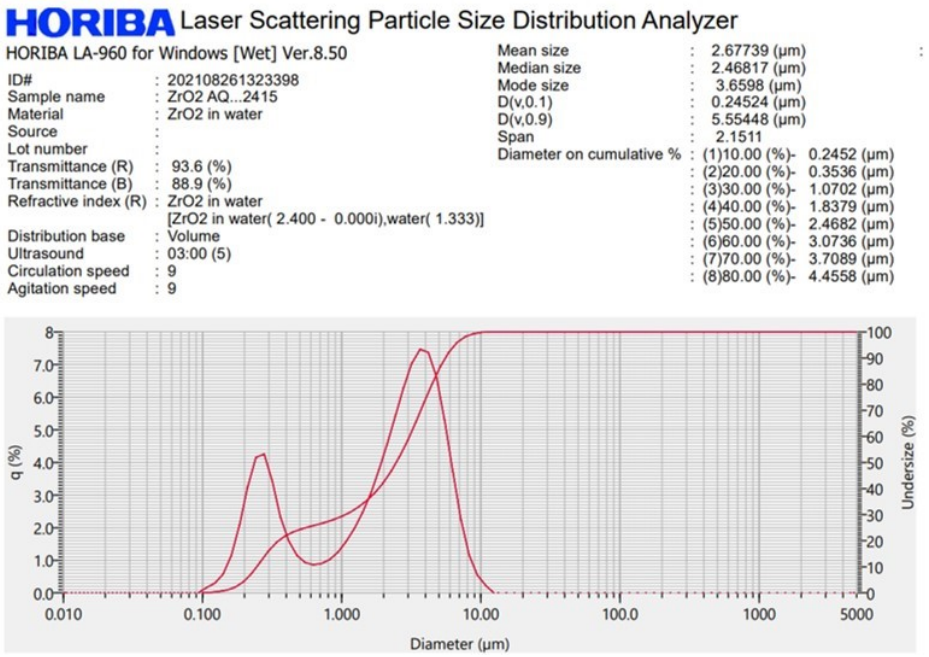

Figure 29: As received ZrO_2 particle size

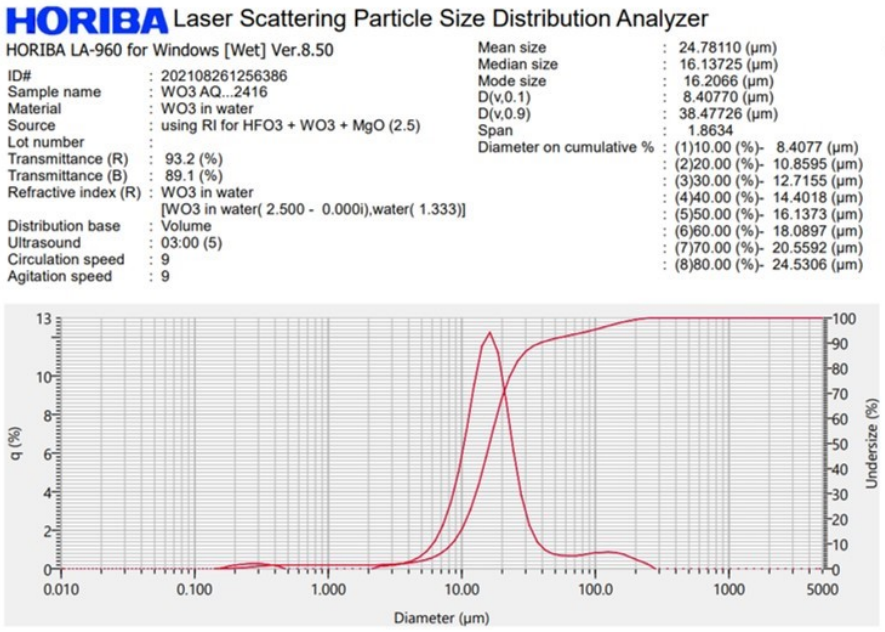

Figure 30: As received WO_3 particle size

HORIBA Laser Scattering Particle Size Distribution Analyzer

HORIBA LA-960 for Windows [Wet] Ver.8.50

ID#	: 202111021500709	Mean size	: 55.49810 (µm)
Sample name	: MgO in Ethanol	Median size	: 12.10148 (µm)
Material	: MgO in Ethanol	Mode size	: 107.8307 (µm)
Source	:	D(v,0.1)	: 3.77803 (µm)
Lot number	:	D(v,0.9)	: 139.26492 (µm)
Transmittance (R)	: 95.0 (%)	Span	: 11.1959
Transmittance (B)	: 92.1 (%)	Diameter on cumulative %	: (1)10.00 (%)- 3.7780 (µm)
Refractive index (R)	: MgO		: (2)20.00 (%)- 5.2564 (µm)
	[MgO(1.734 - 0.000i),ethanol(1.360)]		: (3)30.00 (%)- 6.6684 (µm)
Distribution base	: Volume		: (4)40.00 (%)- 8.4890 (µm)
Ultrasound	: 03:00 (5)		: (5)50.00 (%)- 12.1015 (µm)
Circulation speed	: 9		: (6)60.00 (%)- 70.1077 (µm)
Agitation speed	: 9		: (7)70.00 (%)- 93.1371 (µm)
			: (8)80.00 (%)- 111.9604 (µm)

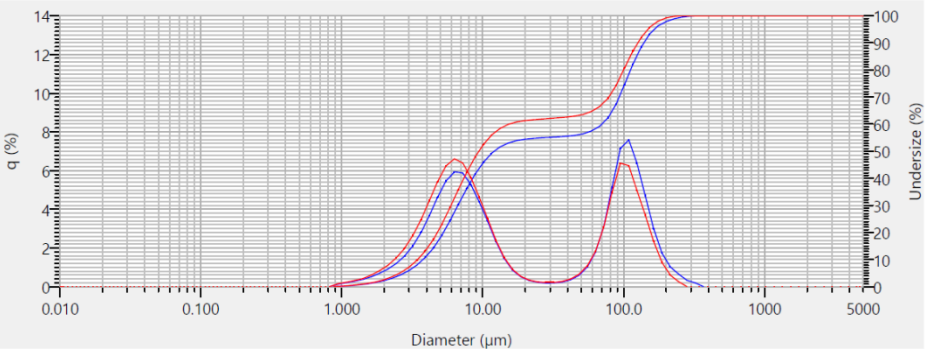

Figure 31: As received MgO particle size

HORIBA Laser Scattering Particle Size Distribution Analyzer

HORIBA LA-960 for Windows [Wet] Ver.8.50

ID#	: 202111021447699	Mean size	: 30.14160 (µm)
Sample name	: HFO2 in DI H2O	Median size	: 23.64105 (µm)
Material	: HFO2 in DI H2O	Mode size	: 42.2432 (µm)
Source	:	D(v,0.1)	: 2.54015 (µm)
Lot number	:	D(v,0.9)	: 65.75087 (µm)
Transmittance (R)	: 94.4 (%)	Span	: 2.6738
Transmittance (B)	: 89.7 (%)	Diameter on cumulative %	: (1)10.00 (%)- 2.5401 (µm)
Refractive index (R)	: Hf2O		: (2)20.00 (%)- 6.3787 (µm)
	[Hf2O(2.104 - 0.010i),Water(1.333)]		: (3)30.00 (%)- 10.2386 (µm)
Distribution base	: Volume		: (4)40.00 (%)- 15.4436 (µm)
Ultrasound	: 03:00 (5)		: (5)50.00 (%)- 23.6411 (µm)
Circulation speed	: 9		: (6)60.00 (%)- 32.7462 (µm)
Agitation speed	: 9		: (7)70.00 (%)- 41.3379 (µm)
			: (8)80.00 (%)- 51.0233 (µm)

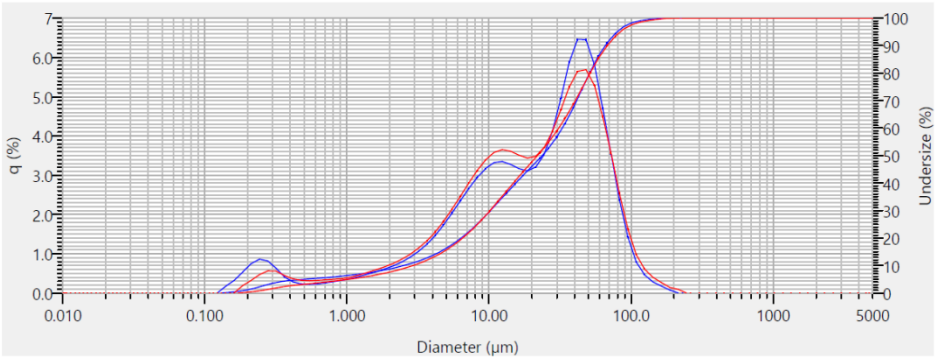

Figure 32: As received HfO_2 particle size

HORIBA Laser Scattering Particle Size Distribution Analyzer

HORIBA LA-960 for Windows [Wet] Ver.8.50

ID#	: 202111021522724	Mean size	: 14.92234 (µm)
Sample name	: Sc2O3 in DI H2O	Median size	: 9.98503 (µm)
Material	: Sc2O3in DI H2O	Mode size	: 10.7598 (µm)
Source	:	D(v,0.1)	: 5.38680 (µm)
Lot number	:	D(v,0.9)	: 18.41116 (µm)
Transmittance (R)	: 94.5 (%)	Span	: 1.3044
Transmittance (B)	: 94.7 (%)	Diameter on cumulative %	: (1)10.00 (%)- 5.3868 (µm)
Refractive index (R)	: Sc2O3 in DI H2O		: (2)20.00 (%)- 6.7313 (µm)
	[Sc2O3 in DI H2O(1.900 - 0.000i),water(1.333)]		: (3)30.00 (%)- 7.8184 (µm)
Distribution base	: Volume		: (4)40.00 (%)- 8.8846 (µm)
Ultrasound	: 03:00 (5)		: (5)50.00 (%)- 9.9850 (µm)
Circulation speed	: 9		: (6)60.00 (%)- 11.1890 (µm)
Agitation speed	: 9		: (7)70.00 (%)- 12.6357 (µm)
			: (8)80.00 (%)- 14.6087 (µm)

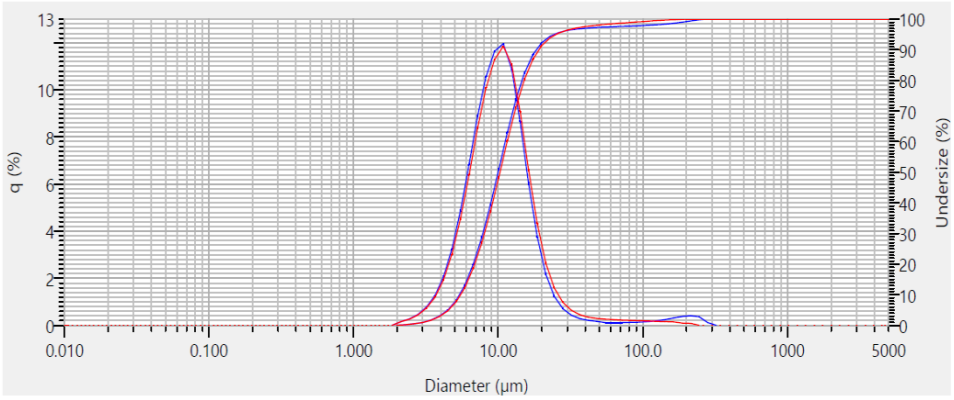

Figure 33: As received Sc_2O_3 particle size

HORIBA Laser Scattering Particle Size Distribution Analyzer

HORIBA LA-960 for Windows [Wet] Ver.8.50

ID#	: 202111021432689	Mean size	: 12.75214 (µm)
Sample name	: Al2O3 in water	Median size	: 8.61028 (µm)
Material	: Al2O3 in water	Mode size	: 8.2339 (µm)
Source	: Al2O3 RI	D(v,0.1)	: 4.47277 (µm)
Lot number	:	D(v,0.9)	: 20.71632 (µm)
Transmittance (R)	: 92.5 (%)	Span	: 1.8865
Transmittance (B)	: 92.8 (%)	Diameter on cumulative %	: (1)10.00 (%)- 4.4728 (µm)
Refractive index (R)	: Al2O3 in DI H2O		: (2)20.00 (%)- 5.5991 (µm)
	[Al2O3 in DI H2O(1.660 - 0.000i),water(1.333)]		: (3)30.00 (%)- 6.5849 (µm)
Distribution base	: Volume		: (4)40.00 (%)- 7.5536 (µm)
Ultrasound	: 03:00 (5)		: (5)50.00 (%)- 8.6103 (µm)
Circulation speed	: 9		: (6)60.00 (%)- 9.8516 (µm)
Agitation speed	: 9		: (7)70.00 (%)- 11.4295 (µm)
			: (8)80.00 (%)- 13.9425 (µm)

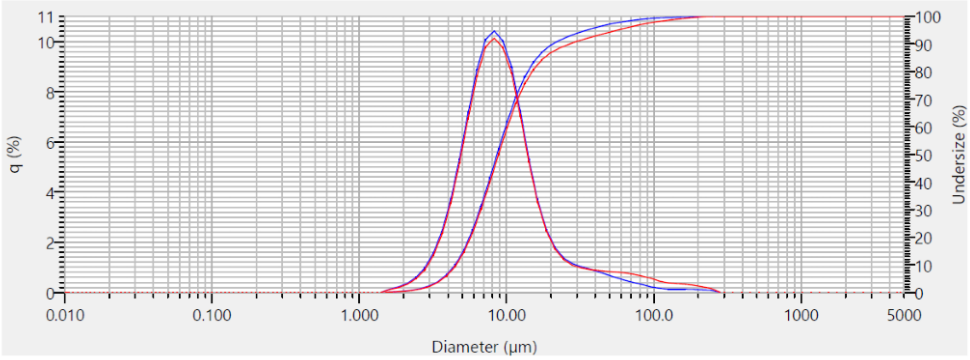

Figure 34: As received Al_2O_3 particle size

A.2. ZrO_2 and WO_3 particle size reduction

~300 g total of ZrO_2 and WO_3 these powders were added in a ratio to form ZrW_2O_8 into a 1 L bottle ½ filled with 5 mm cylindrical YSZ media (Advanced Materials (4039GM-C05)) and then filled 2/3 full with DI water, and placed on a ball mill with the speed adjusted to maximize the sound of milling. The particle size was periodically checked and the d_{90} (90% particles less than reported diameter) is reported in Figure 35 and the size distributions are in Figure 36. A smaller batch (250 mL bottle) using 10 mm media is also shown in Figure 35 for comparison. The large WO_3 particles are clearly ground down quickly within the first day, as are many ZrO_2 particles. With about 4 days of milling, the milling efficiency drops off and the particles reach a steady state size of ~0.1 - 0.2 µm. The steady state size reached for the 10 mm media is larger, as expected.

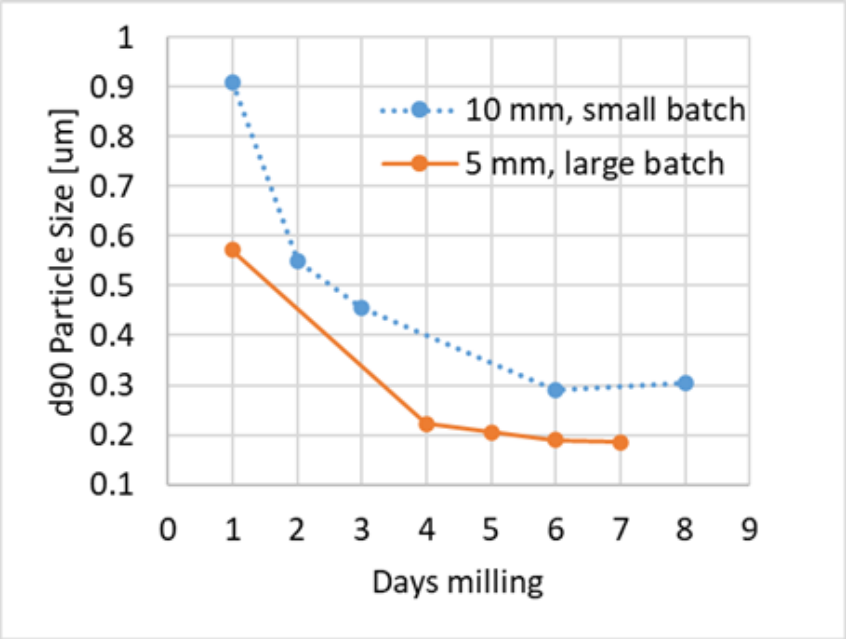

Figure 35: d_{90} particle size reduction for milling ZrO_2 and WO_3.

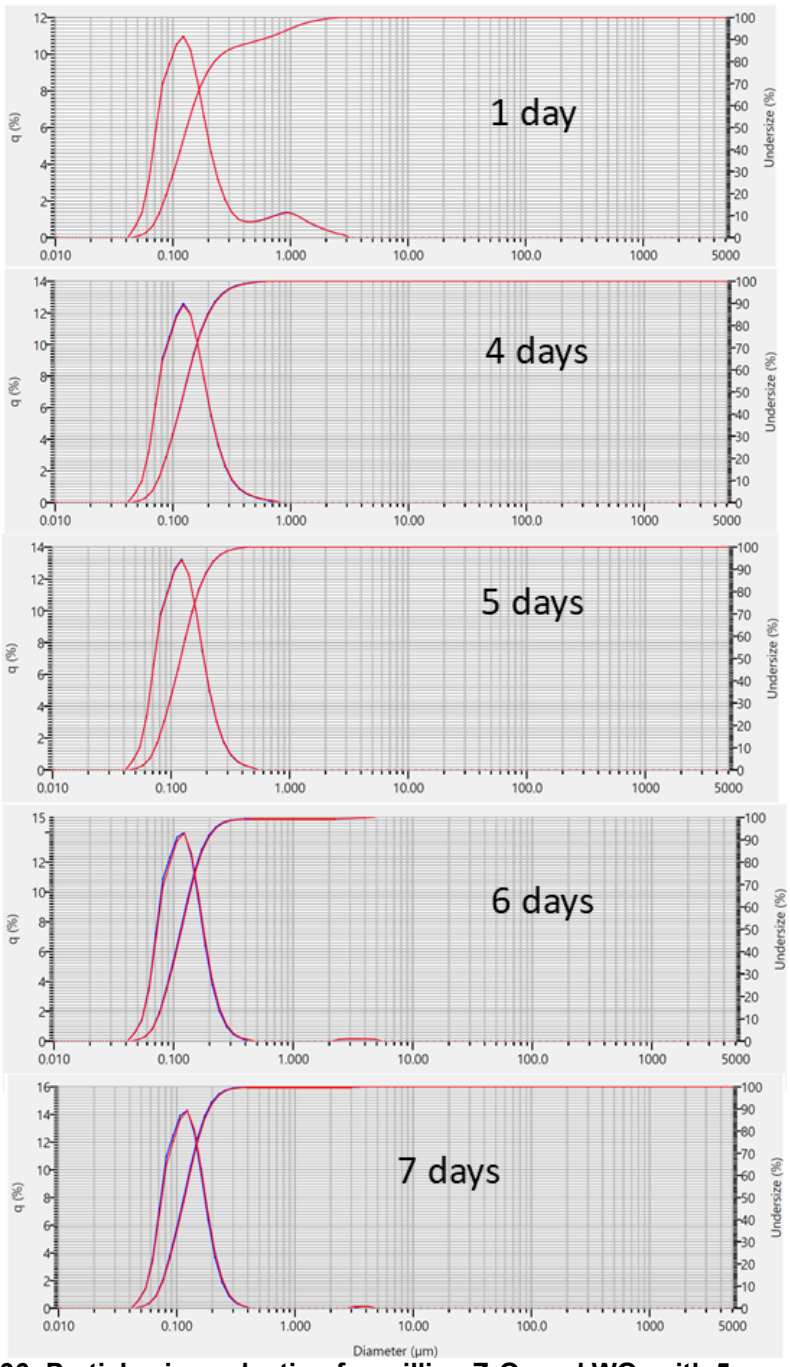

Figure 36: Particle size reduction for milling ZrO_2 and WO_3 with 5 mm media.

A.3. $Al_{0.5}Sc_{1.5}W_3O_{12}$ particle size reduction

As described in the powder fabrication section, $Al_{0.5}Sc_{1.5}W_3O_{12}$ was fabricated in a ~1 kg batch via pressing pellets of mixed oxide precursors and calcining the pellets. The pellets were then broken with a hammer and milled using a turbula mill. The powder size after passing the turbula milled powder through an 850 µm sieve is shown in Figure 37. The turbula milled powder was then ball milled for 7 days, with the final particle size shown in

HORIBA Laser Scattering Particle Size Distribution Analyzer

HORIBA LA-960 for Windows [Wet] Ver.8.50

ID#	: 202207211138129	Mean size	: 14.63679 (µm)
Sample name	: 7/6/22 turbula milled only from pellets p6-38 2 weeks mill	Median size	: 9.23601 (µm)
Material	: WO3 in water	Mode size	: 10.8368 (µm)
Source	: using RI for HFO3 + WO3 + MgO (2.5)	D(v,0.1)	: 1.72449 (µm)
Lot number	:	D(v,0.9)	: 27.16524 (µm)
Transmittance (R)	: 93.3 (%)	Span	: 2.7545
Transmittance (B)	: 92.3 (%)	Diameter on cumulative %	: (1)10.00 (%)- 1.7245 (µm)
Refractive index (R)	: WO3 in water		: (2)20.00 (%)- 3.5110 (µm)
	[WO3 in water(2.500 - 0.000i),water(1.333)]		: (3)30.00 (%)- 5.4712 (µm)
Distribution base	: Volume		: (4)40.00 (%)- 7.3355 (µm)
Ultrasound	: 03:00 (5)		: (5)50.00 (%)- 9.2360 (µm)
Circulation speed	: 9		: (6)60.00 (%)- 11.3405 (µm)
Agitation speed	: 9		: (7)70.00 (%)- 13.9372 (µm)
			: (8)80.00 (%)- 17.8221 (µm)

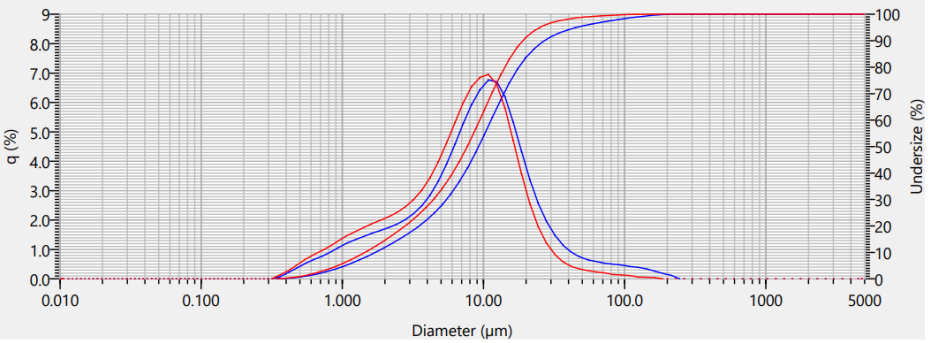

Figure 37: Particle size of turbula milled $Al_{0.5}Sc_{1.5}W_3O_{12}$

HORIBA Laser Scattering Particle Size Distribution Analyzer

HORIBA LA-960 for Windows [Wet] Ver.8.50

ID#	: 202208021218175	Mean size	: 0.55761 (µm)
Sample name	: AlSc Tungstate Aug 2 2022	Median size	: 0.41163 (µm)
Material	: WO3 in water	Mode size	: 0.3661 (µm)
Source	: using RI for HFO3 + WO3 + MgO (2.5)	D(v,0.1)	: 0.20836 (µm)
Lot number	:	D(v,0.9)	: 1.00091 (µm)
Transmittance (R)	: 95.4 (%)	Span	: 1.9254
Transmittance (B)	: 87.9 (%)	Diameter on cumulative %	: (1)10.00 (%)- 0.2084 (µm)
Refractive index (R)	: WO3 in water		: (2)20.00 (%)- 0.2720 (µm)
	[WO3 in water(2.500 - 0.000i),water(1.333)]		: (3)30.00 (%)- 0.3200 (µm)
Distribution base	: Volume		: (4)40.00 (%)- 0.3642 (µm)
Ultrasound	: 03:00 (5)		: (5)50.00 (%)- 0.4116 (µm)
Circulation speed	: 9		: (6)60.00 (%)- 0.4692 (µm)
Agitation speed	: 9		: (7)70.00 (%)- 0.5493 (µm)
			: (8)80.00 (%)- 0.6833 (µm)

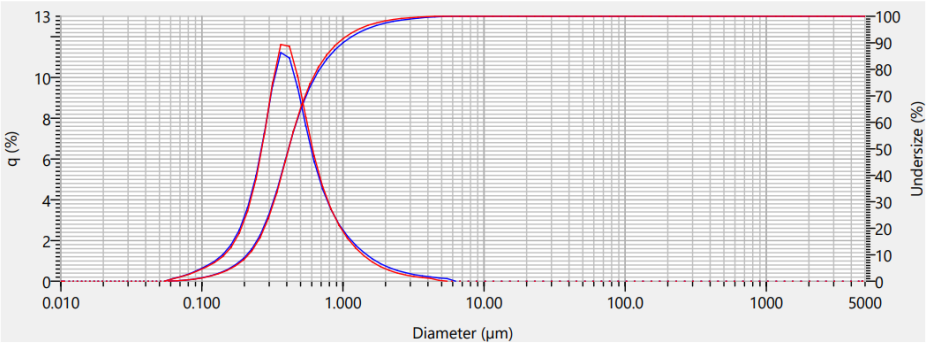

Figure 38: Particle size of 7 day ball milled $Al_{0.5}Sc_{1.5}W_3O_{12}$ from turbula milling.

DISTRIBUTION

Email—Internal

Name	Org.	Sandia Email Address
Charlie Richardson	491	cbricha@sandia.gov
Shawn Pautz	1341	sdpautz@sandia.gov
Cody Kunka	1344	ckunka@sandia.gov
Chad McCoy	1646	camccoy@sandia.gov
Laura Biedermann	1816	lbieder@sandia.gov
Sean Bishop	1816	srbisho@sandia.gov
Mia Blea-Kirby	1816	mablea@sandia.gov
Eric Coker	1816	encoker@sandia.gov
Dan Lowry	1816	drlowry@sandia.gov
Amanda Peretti	1816	asperet@sandia.gov
Perla Salinas	1816	pasalin@sandia.gov
Ed Arata	1831	erarata@sandia.gov
Mark Rodriguez	1819	marodri@sandia.gov
Jacob Mahaffey	1834	jtmahaf@sandia.gov
Shannon Murray	1834	semurr@sandia.gov
Dan Kammler	7585	drkamml@sandia.gov
Margaret Gordon	8923	megord@sandia.gov
LDRD office		ldrd@sandia.gov
Technical Library	1911	sanddocs@sandia.gov

This page left blank

Sandia National Laboratories

Sandia National Laboratories is a multimission laboratory managed and operated by National Technology & Engineering Solutions of Sandia LLC, a wholly owned subsidiary of Honeywell International Inc. for the U.S. Department of Energy's National Nuclear Security Administration under contract DE-NA0003525.